BEAM COUPLING IN HOLOGRAMS STORED IN $LiNbO_3$

by

Randall J. Woods

B.Sc., University of British Columbia, 1974
M.Sc., University of Western Ontario, 1978

A THESIS SUBMITTED IN PARTIAL FULFILLMENT OF
THE REQUIREMENTS FOR THE DEGREE OF
MASTER OF APPLIED SCIENCE

in

THE FACULTY OF GRADUATE STUDIES
Department of Electrical Engineering

UNIVERSITY OF BRITISH COLUMBIA

We accept this thesis as conforming
to the required standard

THE UNIVERSITY OF BRITISH COLUMBIA
July, 1981

© Randall J. Woods

In presenting this thesis in partial fulfilment of the requirements for an advanced degree at the University of British Columbia, I agree that the Library shall make it freely available for reference and study. I further agree that permission for extensive copying of this thesis for scholarly purposes may be granted by the head of my department or by his or her representatives. It is understood that copying or publication of this thesis for financial gain shall not be allowed without my written permission.

Department of Electrical Engineering

The University of British Columbia
2075 Wesbrook Place
Vancouver, Canada
V6T 1W5

Date 12/8/81

DE-6 (2/79)

ABSTRACT

The potential use of photorefractive crystals in optical data handling applications has received considerable attention during the past decade. The photorefractive effect in $LiNbO_3$:Fe involves the photoliberation and inhomogeneous redistribution of electrons which are subsequently trapped in the new distribution. The resulting electric fields set up a similar distribution of variations in the refractive index allowing the formation of thick phase holograms.

In the case of an elementary hologram (that written by a simple interference pattern between two equal intensity beams of monochromatic light), the holographic grating may be displaced from the fringe pattern that wrote it. This phase shift gives rise to a redistribution of energy between the two beams, called beam coupling. Measurements of the beam coupling can be used to obtain a value for the phase shift, and this in turn is useful in studying the electron transport mechanisms which give rise to the shift. Previous attempts to measure the beam coupling have not yielded reproducible results and have consequently not been very useful in determining the phase shift or studying it causes.

The present set of experiments have shown that the phase shift is not constant in time during the writing process, and repeated measurements as the hologram was written showed that this variation is a linear function of time for any particular experiment. The causes of this variation can be attributed to the nature of the writing process, thermal expansion and mechanical creep of the optical components. Repeated experiments showed that the value of the shift extrapolated to t=0 of the writing process was a constant for the crystal used. Because the holograms were written under conditions which made the bulk photovoltaic effect the dominant process, it was possible to calculate the transport length due to this effect. The value arrived at was 13 ± 3 nm.

TABLE OF CONTENTS

LIST OF VARIABLES

A	amplitude of subject beam with reference normalized
BPE	"bulk photovoltaic effect"
d	crystal thickness
d_{ijk}	piezoelectric moduli (d_{ij}, contracted form)
D, D_i	dielectric displacement vector, tensor element
E	applied electric field
EO	"electro-optic"
E_{sc}	field due to space charge in crystals
E_v	virtual field
E_D	drift field
f_1, f_2	real constants (eq. 6.4, 6.6)
FP	"fringe pattern"
g(x)	volume generation rate of free electrons
g_o	constant of generation rate equation (eq. 6.6)
HG	"holographic grating"
i_{ph}	photocurrent
I	light beam intensity
I_R, I_s	transmitted reference and subject beam intensities (eq. 3.8)
J_{ph}	photocurrent density (eq. 4.1)
J_o	average conduction current density (eq. 6.11)
J_{e1}, J_{e2}, J_r	see eq. 4.1
k	fringe pattern grating vector
ℓ	fringe spacing in HG
$\ell_+ \ell_- \ell_+' \ell_-'$	electron mean free paths (eq. 5.2-5.4)
$\Delta \ell_i$	displacement of i^{th} ion (eq. 5.3)

L	length of crystal along c-axis (eq. 6.10)
L_p	electron transport length due to BPE
L_d	diffusion transport length
m	modulation rato (eq. 6.1)
m'	effective modulation rato (eq. 5.11 a,b,c)
n	index of refraction, $n_i = \sqrt{\varepsilon_{ii}}$
Δn	see eq. 3.1
n_1	amplitude of index modulation in grating
n_o/n_e	ordinary/extraordinary index of refraction
N	impurity concentration
p,p'	scattering probabilities (eq. 5.11c)
$p_+p_-p_+'p_-'$	probabilities (eq. 5.11c)
P_i	polarization tensor
ΔP	change in spontaneous polarization
q	unit charge
r	amplitude of reference wave
R	reference beam (eq. 3.3)
R_I	$=(r/s)^2$
R_{mn}	contracted quadratic EO matrix element
$R_{ijk\ell}$	quadratic EO matrix element
r_{mk}	contracted linear EO matrix element
s	amplitude of signal (subject) wave
S	subject beam (eq. 3.3)
$S(\Omega)$	photo-ionization cross section (eq. 5.7)
V	fringe visibility (voltage)
x	unit vector (figure 2.2)
z	unit vector (figure 2.2)

z_i	charge on the i^{th} ion (eq. 5.3)
z_{ijk}	linear EO coefficient
α	crystal light absorption constant
ε	permittivity of first space
ε_{ij}	tensor relative permittivity (strain matrix in Appendix B)
η	grating diffraction efficiency
θ	angle of incident beam relative to crystal normal inside crystal
θ_o	as above outside crystal
θ_p	angle of incidence of beams from normal to mirrors M_5,M_6
κ	anisotropy constant (eq. 4.1)
κ_g	grating coupling constant (eq. 3.4)
λ	optical wavelength inside crystal
λ_o	optical wavelength in freespace
μ_{12}	degree of coherence between two interfering beams
ξ	quantum efficiency
ρ	electron density
ρ_L,ρ_D	crystal electron density in light, dark
ρ_{sc}	trapped charge density
σ_{jk}	stress tensor (σ_j, contracted form)
τ	free electron lifetime
ϕ	phase of reference beam with respect to subject beam, or equivalently, phase mismatch between HG and FP
ϕ_p	phase shift due to BPE
ϕ_d	phase shift due to finite diffusion transport length
ω	optical frequency
Ω	angle between direction of polarization of two interfering beams.

LIST OF FIGURES

ACKNOWLEDGEMENTS

I would like to thank Dr. Lawrence Young for suggesting the research topic and for his guidance during the course of the research.

Thanks also to Al MacKenzie for help with the drafting and Kathy Brindamour and Gail Hrehorka for preparing the manuscript.

1. INTRODUCTION

It is possible (Chen et al., 1968) to store pure phase holograms in certain ferroelectric crystals. Physically, the hologram is composed of a refractive index distribution with the variation in the index being typically one part in 10^5 and effecting the reproduction of a holographic image through Bragg diffraction of the reference beam. The storage of the original light diffraction pattern as a refractive index distribution is a result of the photorefractive effect. In brief, this effect is brought about by the photoliberation of electrons in traps within the crystal, which then migrate under drift, diffusion and a process called the bulk photovoltaic effect. Through successive excitations and re-entrapments, the electrons approach an inhomogeneous distribution which is determined by the light diffraction pattern and certain characteristics of the transport mechanisms. The resulting electric field distribution results in a refractive index distribution due to the electro-optic effect, and this becomes the physical recording of the hologram. This recording may be subsequently removed by uniform illumination or heating of the crystal, which removes the refractive index modulation through optical or thermal excitation and uniform redistribution of the electrons.

Staebler and Amodei (1972) noted that if the fringe pattern formed by two interfering plane waves is laterally displaced from a diffraction grating upon which the fringes are incident, then the two beams will become coupled. This results in a trading of energy between them (Ch. 3).

There are several processes which could result in the hologram grating being shifted by some phase angle with respect to the fringe pattern. Young et al. (1979) showed that a phase shift of from 0 to $\pi/2$ radians can arise if drift is an important means of electron transport. The transport length due to the bulk photovoltaic effect can also result in a phase shift,

depending on the value of the transport length with respect to the grating line spacing. (More correctly, a thick phase hologram has a "plane spacing", but the more common term is used here.)

The beam coupling arising from the phase shift due to the bulk photovoltaic effect can be studied by either allowing for other sources of shift in subsequent calculations or devising an experimental arrangement in which they are negligible. There have been several reported attempts to study the nature of this coupling and draw conclusions concerning the processes which give rise to it, but to date there has been considerable difficulty in achieving reproducible results. The object of the present work was to further investigate the coupling with an aim to determining the sources of difficulty and whether they could be avoided by changes in the apparatus, or their effects circumvented by appropriate data analysis.

From an engineering standpoint, the ultimate goal of investigations such as this into the physical processes at work in ferroelectric crystals during illumination is to enable the design and construction of electro-optic devices using these materials. The main application of these devices will be in the general area of data handling and will make use of the high speed and relative immunity to electrical interference offered by optical rather than electrical transmission. Specific applications include two and three dimensional displays, pattern and character recognition image processing, holographic interferometry and holographic data storage. These are discussed in Appendix D.

2. OPTICAL HOLOGRAPHY

During the three decades since its inception, wavefront reconstruction, or holography, has undergone considerable development and seen an increasingly broad range of application. It is characterized, in its simplest form, by the formation of a recorded image which is not the object's image, but rather the interference pattern between the object's incoming wavefront and that of a phase related second beam called the reference beam, which is often (but not necessarily) a plane wave. After the image has been formed on the recording medium, shining only the reference on it results in the reconstruction of the original object's image, which will exhibit the depth and parallax properties normally associated with that object (from a limited angle of view). This is possible because, unlike a common photograph which preserves only amplitude information along the surface occupied by the film, the hologram is an interference pattern between two phase related beams, from which both the original amplitude and phase information can be recorded (Fig. 2.1).

One can see how this is accomplished by first considering an elementary hologram made by recording the interference pattern formed by the intersection of two plane, non-parallel, monochromtic and phase-related beams of the same amplitude (Fig. 2.2). As the diagram shows, this results in a plane grating with the grating vector perpendicular to the beam bisector and in the plane of the two beams. The general and more complex case of the interference of two arbitrary wavefronts can be looked at as just the sum of the interference patterns of all the plane waves constituting their Fourier components.

The formation of a hologram and the description of several of its characteristics depends upon the degree of coherence of the illumination. It is useful to divide the topic of coherence into two parts: spatial (lateral)

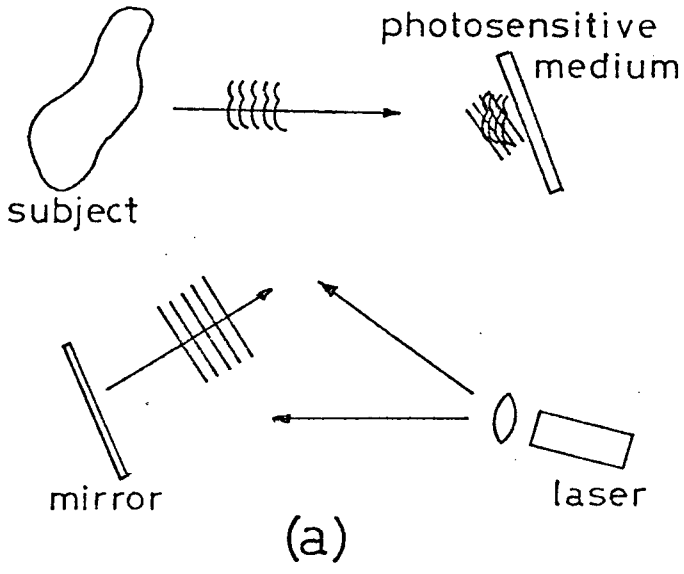

FIGURE 2.1

Simple hologram writing and reading geometries. "a" shows the presence of both the reference and subject beams, which form an interference pattern on the recording medium. "b" shows the reading geometry in which the object beam is absent but is reconstructed via diffraction of the reference beam.

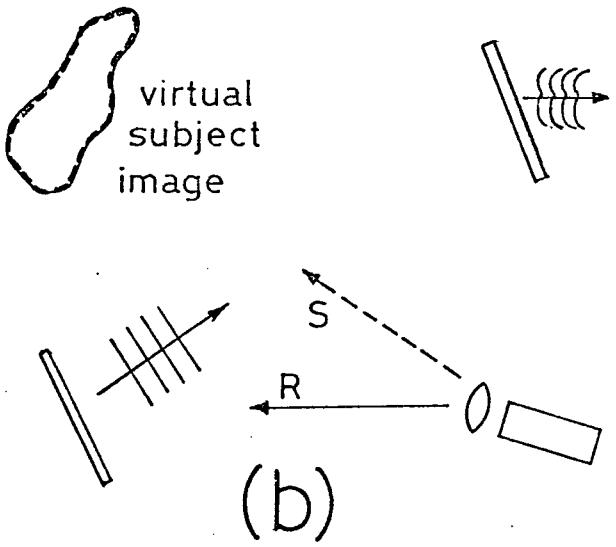

FIGURE 2.2

An elementary hologram formed in a medium of thickness 'd' (as viewed from the top in these experiments).

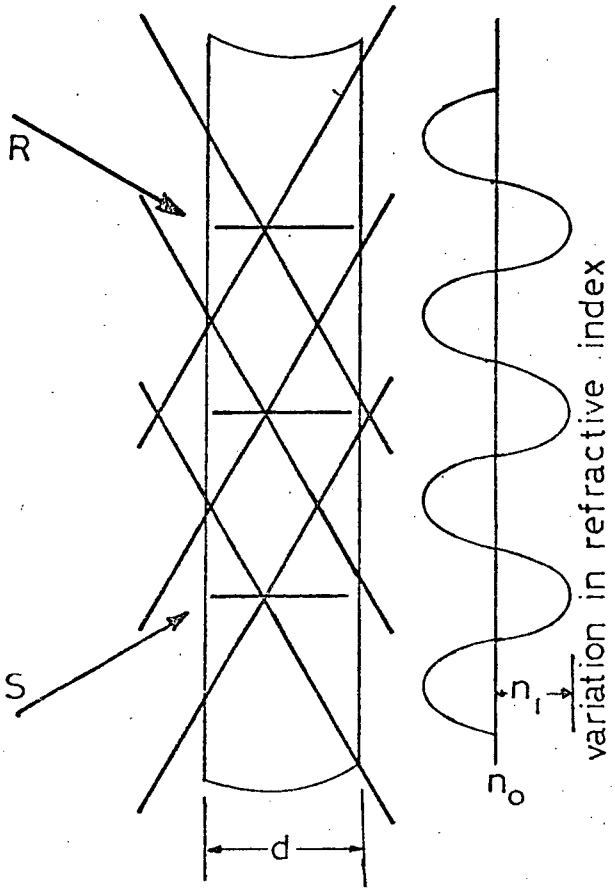

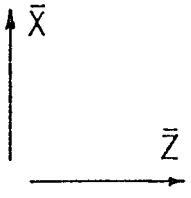

coherence, and temporal (longitudinal) coherence. Most commercial gas lasers oscillate (or can be so adjusted) only in the lowest transverse mode (TEM_{00}). As a consequence, they are spatially coherent, and so this is not a problem when writing holograms with them. This means that the light at any point on a plane normal to the direction of propagation is in phase with any other point on the plane, and thus the entire width of the beam is useful for the purpose of writing a holgram.

The spectral purity of a laser's radiation is closely related to its degree of its temporal coherence. Though a laser oscillating in only one longitudinal mode possesses ideal temporal coherence, several modes are generally present. The (longitudinal) coherence length, ΔL_H, determines the distance along the beam axis between points which are still coherent. If the phase path lengths of two split beams differ by more than the coherence length they will not exhibit interference fringes when brought together, and thus a hologram will not be formed.

To attain high diffraction efficiencies, it is necessary that the optical system be arranged to display optimal fringe visibility, V, or standing wave ratio, which is of the form

$$V = \frac{I_{max} - I_{min}}{I_{max} + I_{min}}$$

where I_{max} and I_{min} are the maximum and minimum intensities of the interference fringes. V is, in general, a function of the degree of coherence $|\mu_{12}(\tau)|$ between the two interfering beams, the angle Ω between the directions of polarization of the two beams, and the ratio R_I of the intensities of the two beams ($R_I \leq 1$) as follows

$$V = \frac{2|\mu_{12}(\tau)|\sqrt{R_I}\cos\Omega}{R_I + 1}$$

The geometry of the present set of experiments is such that $\Omega=0°$ and $|\mu(\tau)| = 1$ and thus for our purposes

$$V = \frac{2\sqrt{R_I}}{R_I+1} \qquad \text{where} \quad R_I = (r/s)^2$$

r,s = amplitudes of reference and signal waves

To optimize V it is seen that we must make R_I unity at all points in the diffraction pattern, which, in the experimental setup used, means that we must have an axially symmetric beam, preferably of Gaussian cross-section. This is achieved by spatial frequency filtering. The beam is brought to a point focus by a lens and passed through a pinhole at that point, thus allowing through only the very lowest spatial frequencies characteristic of the slowly varying Gaussian distribution, and blocking the higher spatial frequencies characteristic of noise. A following lens is used to collimate the spherical wave emerging from the hole (Fig. 2.3). It can be shown that a pinhole diameter of the order of 10 μm will filter out noise from such sources as multiple reflections from lenses and diffraction rings from dust spots.

A beam splitter is required to divide the laser beam into a subject and reference wave. The two methods available are amplitude division and wavefront division, as shown in Fig. 2.4. The former is generally preferred because it requires less beam expansion and provides more uniform illumination. A further choice to be made is whether to split the beam before or after filtering. The advantages of the former are that it (1) requires a smaller splitter aperture and (2) the noise from the splitter is filtered. The second option, however, requires only one set of beam expanding optical elements.

It is essential to the formation of a sharp holographic image that the interference fringe pattern remain fairly stationary with respect to the

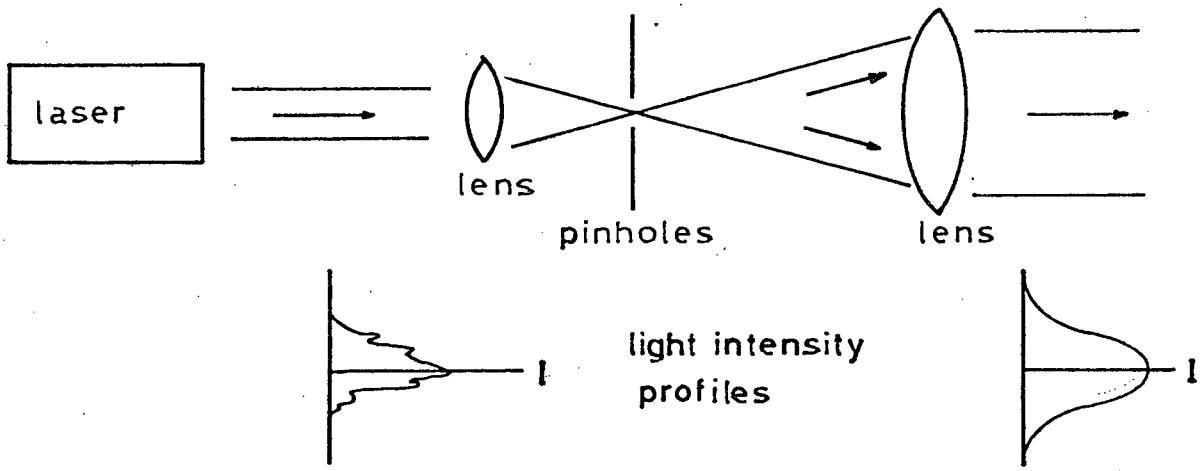

FIGURE 2.3

Effect of a spatial filter on the light intensity profile.

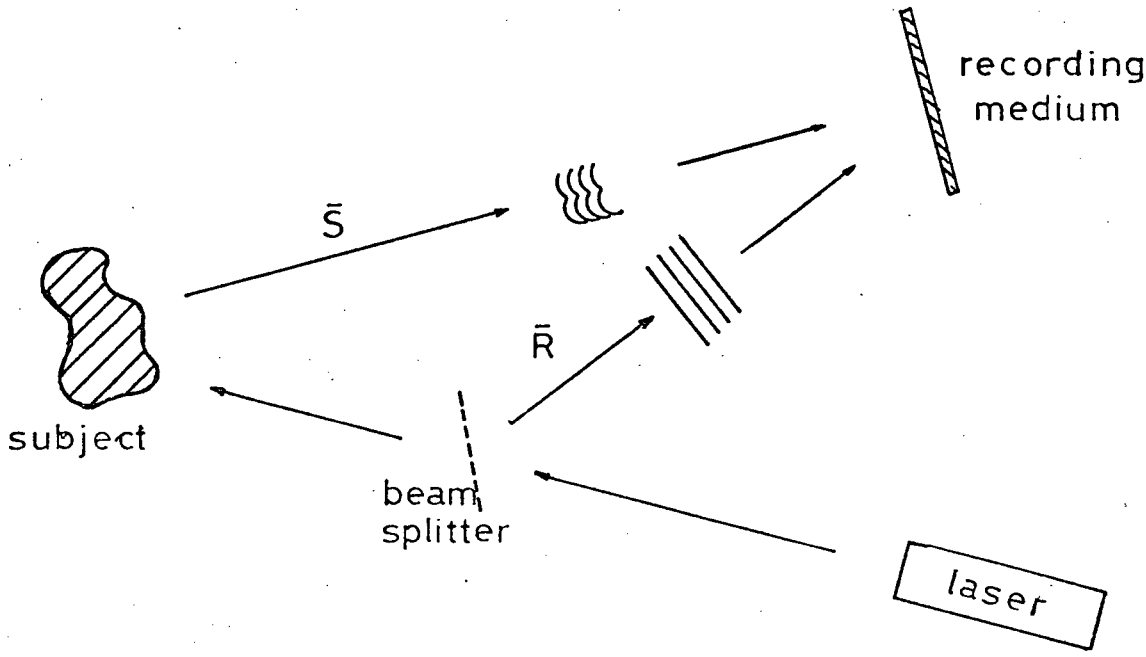

FIGURE 2.4

Hologram geometry using amplitude division (as opposed to wavefront division shown in Fig. 2.1a).

recording medium throughout the duration of the process. In general, one must minimize the total time that the magnitude of bench vibrations exceeds the highest spatial frequency in the pattern being recorded, which is usually taken to be the wavelength of the light being used. In the present work, relating the degree of beam coupling to the relative positions of the fringe pattern to the hologram grating required even greater care to prevent random variations in their position. Massive tables, often made of granite, concrete or steel and resting on sand, pneumatic supports, etc. are often used to filter out building vibrations. Airborne thermal and acoustic disturbances, especially in the beam paths between the beam splitter and recording medium must be minimized by eliminating the source of the disturbance or, often more practically, protecting the setup from it. In the current set of experiments, a Michelson interferometer was included as part of the system in order to provide continuous monitoring of this occasionally troublesome problem.

3. DIFFRACTION OF COUPLED WAVES

This chapter deals with the theory of the interaction of one or two incident beams of light with a sinusoidal thick phase grating (Staebler and Amodei, 1972). Though the development given here yields useful results, it will be seen later that its application is not generally applicable to holograms written in $LiNbO_3$, but rather is restricted to certain conditions.

Consider a sinusoidal grating (an elementary thick phase transmission hologram) in a crystal of thickness d (Figure 3.1):

$$\Delta n = n_1 \cos \left[(2\pi/\ell)x\right] \quad . \tag{3.1}$$

Two coherent beams of light, R and S, are symmetrically incident upon the surface so that they make an angle θ relative to the Z-axis inside the crystal. We assume that perfect Bragg conditions prevail so that the relationship between the optical wavelength λ in the crystal and the phase grating wavelength ℓ is given by

$$\lambda = 2\,\ell \sin \theta \tag{3.2}$$

We then write

$$\begin{aligned} R &= R(z) \exp \{-i\left[(2\pi \cos \theta/\lambda)z + (\pi/\ell)x\right]\} \\ S &= S(z) \exp \{-i\left[(2\pi \cos \theta/\lambda)z - (\pi/\ell)x\right]\} \end{aligned} \tag{3.3}$$

Applying coupled wave theory (Kogelnik, 1969) we find that the variation of the beams within the volume of the gating is given by the expressions

$$\frac{dR(z)}{dz} = -i\kappa_g S(z) \qquad \frac{dS(z)}{dz} = -i\kappa_g R(z) \tag{3.4}$$

where $\kappa_g = \pi n_1/\lambda \cos \theta$ is the grating coupling constant (not to be confused with the anisotropy constant κ to be introduced later). The general solution to these coupled equations is

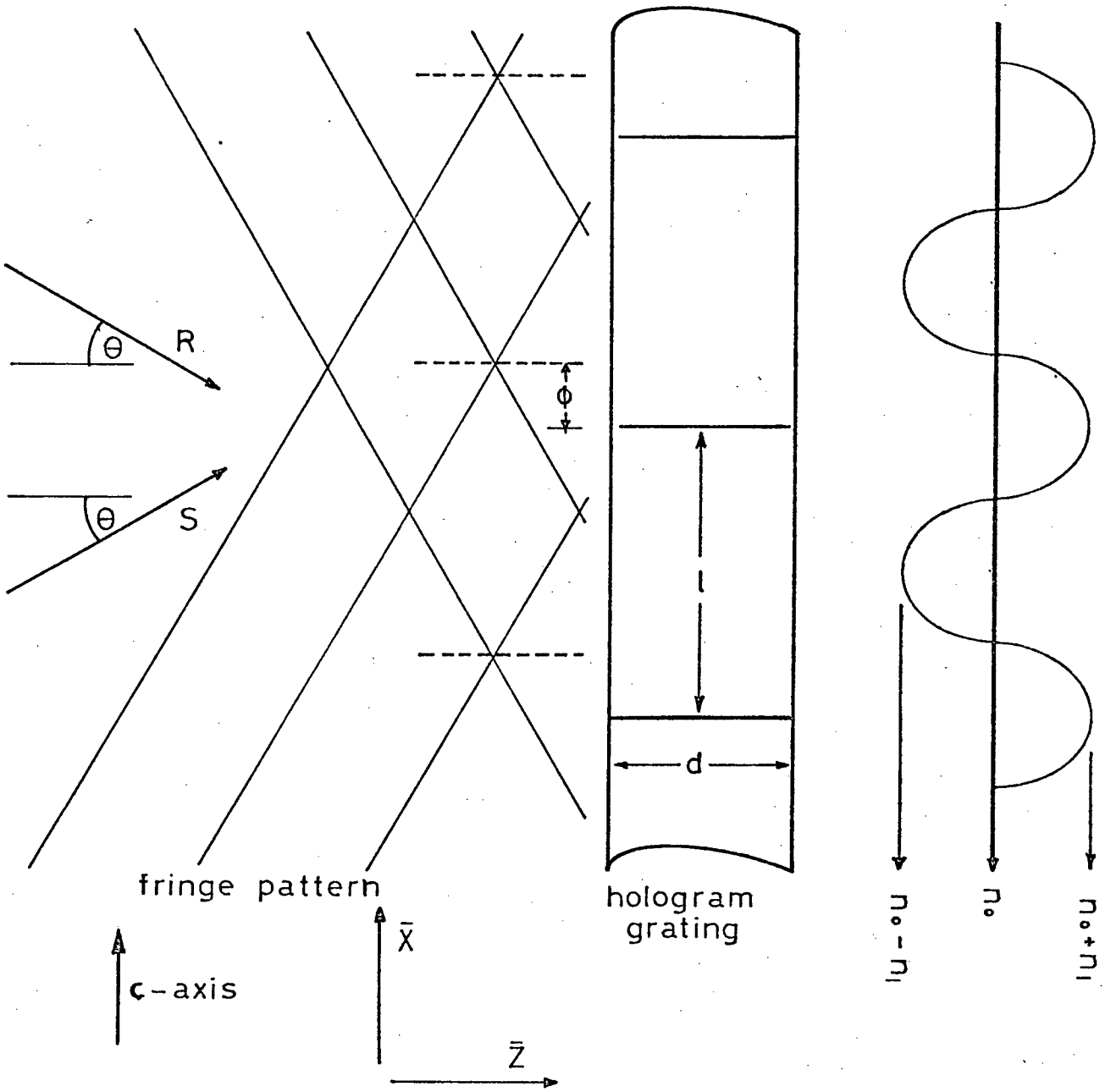

FIGURE 3.1

Fringe pattern caused by interference of R(0)=1 and S(0)=$e^{-i\phi}$ compared to crystal thickness 'd' upon which a hologram grating of spacing 'l' has been written. The fringe pattern is displaced by ϕ along the x-axis from the hologram grating, which is described by equation 3.1. θ is the angle to the crystal normal made by the incident beams inside the crystal.

$$R(z) = ae^{i\kappa_g z} + be^{-i\kappa_g z}$$
$$S(z) = -ae^{i\kappa_g z} + be^{-i\kappa_g z} \qquad (3.5)$$

The coefficients a and b are determined from the boundary conditions at z = 0, i.e. the phase and amplitude of the beam at the first surface of the crystal. In the general case we normalize R(0) = 1 and then set $S(0) = Ae^{-i\phi}$. This gives

$$R(z) = \cos(\kappa_g z) - iAe^{-i\phi}\sin(\kappa_g z)$$
$$S(z) = -i\sin(\kappa_g z) + Ae^{-i\phi}\cos(\kappa_g z) \qquad (3.6)$$

Squaring these we get the intensities,

$$I_R = \cos^2(\kappa_g z) + A^2\sin^2(\kappa_g z) - A\sin(2\kappa_g z)\sin\phi$$
$$I_S = \sin^2(\kappa_g z) + A^2\cos^2(\kappa_g z) + A\sin(2\kappa_g z)\sin\phi \qquad (3.7)$$

Although these equations refer to the case where the grating is fixed and one beam's phase differs from the other's by ϕ, we can also describe the equivalent relationship of fixed beams [R(0) = 1, S(0) = A] and a movable grating given by

$$\Delta n = n_1 \cos[(2\pi/\ell)x + \phi] \quad .$$

The case of beam readout, represented by S(0) = 0 and R(0) = 1, has been well studied and theory agrees with experiment. The more complicated case of beam coupling during writing, which applies in this work, uses the boundary conditions R(0) = 1 and $S(0) = Ae^{-i\phi}$. If the incident beams are balanced (A = 1), the equations (3.7) reduce to

$$I_R = 1 - \sin(2\kappa_g z)\sin\phi$$
$$I_S = 1 + \sin(2\kappa_g z)\sin\phi \qquad (3.8)$$

It is immediately obvious that for the case of $\phi = 0$ (i.e. when the grating

lines up with the fringe pattern), there should be no energy transfer. The case where the grating is displaced along the x-axis from the fringe pattern ($\phi \neq 0$) results in energy transfer, the amount of which depends upon the amount of grating displacement. Qualitatively, a small shift of the grating towards the S-beam side enhances the S-beam, and vice-versa. Also, the strength of the grating at a particular time influences the amount of coupling, as is shown in the sin $(2\kappa_g z)$ factor in the last term. This is related to the diffraction efficiency of the grating by (Staebler and Amodei, 1972)

$$\eta = \sin^2 (\kappa_g z) \qquad \text{(at } z=d\text{)} \tag{3.9}$$

We define η for a lossless crystal as

$$\eta = \frac{I_s(d)}{I_R(0)} = \frac{I_s(d)}{I_s(d) + I_R(d)}$$

where the right hand side is used in these experiments.

The foregoing theory applies to any lossless purely sinusoidal thick phase transmission grating. However, this is only an approximate description of the grating actually formed by illuminating a $LiNbO_3$:Fe crystal with two interfering plane waves, and the description becomes less accurate as the illumination continues. The reason for this lies in the detailed physical nature of the writing mechanism within the crystal. Therefore, before considering the specific case of hologram writing in a $LiNbO_3$ crystal, we will first deal with the basic processes involved, namely the photorefractive effect and the bulk photovoltaic effect.

4. PHOTOREFRACTIVE EFFECT

A number of ferroelectric crystals have been found to undergo minute changes in their indices of refraction upon exposure to sufficiently intense light of an appropriate wavelength. This phenomenon, called the photorefractive effect, was first considered to be something of a nuisance because it led to eventual degradation of performance in early electro-optic (EO) devices using these crystals. However, because they had such desirable (i.e. high) EO coefficients, work was done to find out how to eliminate this problem in the crystals, which led to a better understanding of the effect.

The photorefractive effect takes place in the following manner. Light in the appropriate wavelength range (450-550nm in the case of $LiNbO_3$) incident upon the crystal causes photoexcitation of electrons in deep traps, which are associated with defect sites and impurities. The electrons then migrate under the influence of a number of different mechanisms for some period of time until they are recaptured by traps at other locations within the crystal. Depending upon the intensity pattern of the incident light, the end result will be an uneven redistribution of the electron density, resulting in a pattern of electric fields within the crystal. Finally, the linear EO effect (in which an applied electric field may induce a small change in the index of refraction - see Appendix A) results in this field pattern being translated into a refractive index distribution which is related in some unique fashion to the intensity pattern of incident light.

The trapped charge/refractive index pattern can be removed in at least three ways:

i) by allowing the dark conductivity of the crystal to slowly return the distribution to its original state;

ii) by strongly illuminating the entire crystal with a wavelength to which it is photosensitive (this can be fast, but measures must be taken to ensure that parasitic holograms do not form);

iii) by heating the crystal in an oven (200°C for one hour was found to be effective).

The last method, followed by two hours of gradual cooling in the oven (with the c-axis faces shorted during heating and cooling to control pyroelectric effects) was adopted in this work.

As mentioned above, photoexcitation of electrons in deep traps associated with defect sites and impurities is responsible for making free electrons available for migration under the various processes in effect (Peterson et al., 1972). Stoichiometric defects (geometric lattice irregularities) have been studied (Phillips et al., 1972) by exposing nominally pure $LiNbO_3$ to gamma irradiation. The resulting increase in lattice defects was seen to be accompanied by increased photoconductive sensitivity. The influence of impurities upon the optical properties of photorefractive crystals was first studied to find ways of decreasing the effects upon EO devices developed to make specific use of the photoelectric effect. A number of studies (Phillips et al., 1972, Peterson et al., 1971; Mickami et al., 1973; Glass et al., 1974) showed that doping with iron, manganese, copper and other impurities increase the photorefractive sensitivity, with the most commonly used (and the best found to date) being iron, usually in concentrations of a few hundredths of a mole-percent. The iron is present as Fe^{2+} and Fe^{3+} with the Fe^{2+} possibly being located in oxygen vacancies (Dischler and Rauber, 1975) and the Fe^{3+} being located by Mossbauer effect studies in the niobium sites, though neither of these findings is certain. As the iron impurity's trivalent state (Fe^{3+}) constitutes an empty trap and the divalent state (Fe^{2+}) an occupied trap, one would expect that the oxidation/reduction state of the iron impurities would affect

the photorefractive sensitivity (Staebler and Amodei, 1974 a,b). Annealing $LiNbO_3$ in air or oxygen at 600°C (Peterson et al., 1971) has been shown to be one effective method of oxidizing the Fe^{2+} state to Fe^{3+} (i.e., increasing the number of traps), with as much as 96% of the iron going to the trivalent state (Clark et al., 1973). It has been shown by Cornish (1975) that heating of the crystal to 540°C while packed in Li_2CO_3 powder reduced iron centres to the Fe^{+2} state and destroyed shallow traps, which decreased thermal decay of a hologram while aiding optical writing and erasure. Other methods include field annealing (removing lattice defects to reduce photorefractive sensitivity - Smith et al., 1968) and a process involving the heating of a crystal in contact with a similar but much larger crystal, which alters the composition or non-stoichiometry by lithium oxide transport between the two crystals.

Several attempts to construct a physical model of the photorefractive process have been made during the past decade. Though they all agree with the general description put forward at the beginning of this section (i.e. photo-excitation from traps, migration, anisotropic re-entrapment, resulting space charge fields causing an index change via EO effect), there has been some problem determining the precise nature of the migration. It has been variously attributed to diffusion, drift under the influence of some field, and a new "bulk photo-voltaic effect". Following are summaries of several published models:

i) The Internal Field Model. Chen (1969) attributed the photorefractive effect to drift in the presence of an internal field in the crystal, the origin of which was not clear. His conclusions were based upon adjustable compensator measurements of changes in birefringence induced by a laser beam incident on a small central section of a crystal. As shown in Figure 4.1, it was found that the change in birefringence changed sign along the c-axis, but not

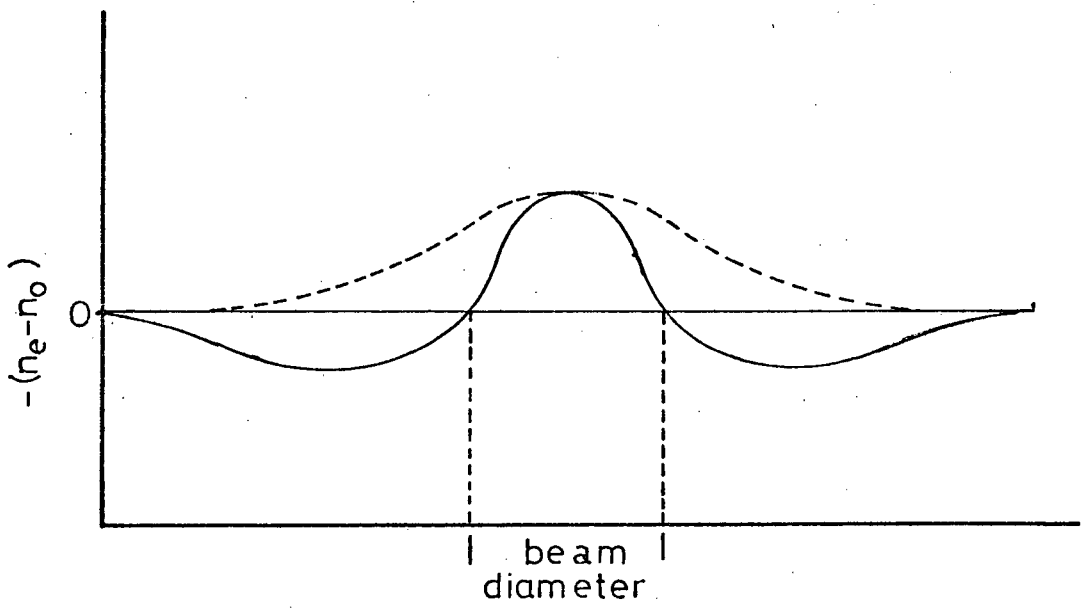

FIGURE 4.1

Change in birefringence induced with a single laser beam in $LiNbO_3$ as observed by Chen (1969). The solid line represents the change along the c-axis due to a radially symmetric beam, and the dashed line the change along the b-axis.

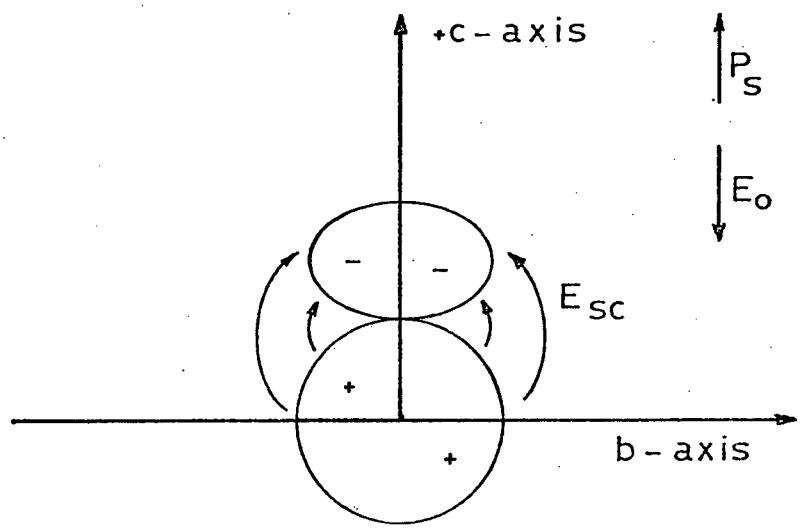

FIGURE 4.2

Space charge field postulated by Chen to account for the observed change in the birefringence.

the b-axis. He assumed an electro-optic effect and postulated (1) the presence of empty traps available to capture electrons and full traps available to donate them upon photo-ionization, and (2) the presence of an internal electric field, E_{in}, directed opposite to the direction of spontaneous polarization. Photoexcited electrons will therefore drift in the direction of the c-axis being repeatedly trapped and re-excited until they are out of the illuminated volume, where they are finally trapped. Thus a space charge develops (Figure 4.2) which results in the creation of an electric field and variation in the index of refraction by the electro-optic effect. Observation of short-circuit photocurrents was considered to be further evidence of the existence of E_{in}. A pyroelectric origin of the field, arising from non-uniform heating of the crystal during illumination, was dismissed because the direction of the photocurrent disagreed with the sign of dP/dT (negative).

ii) The Polarization Model. Johnston (1970) put forward a model in which the photorefractive effect (or more specifically, the as yet unexplained E_{in}) was attributed to photoinduced variations in the macroscopic polarization. In this mechanism, incident light excites electrons into the conduction band (where they are free to move) causing a decrease in the density of filled traps in the illuminated volume and thus a local change in polarization. With the laser off, this change is frozen in and the resultant divergence of the polarization is accompanied by a permanent field which gives rise to a change in index via the EO effect. One of several difficulties with this model is that it does not explain the steady

state, short circuit photocurrent observed in a crystal under full illumination.

iii) Pyroelectric Field Model. A second attempt (Amodei and Staebler 1972 b) to attribute the field to a polarization effect, this time arising during the cooling of the crystal from a high temperature (e.g. during crystal formation) was not supported by experimental results (Cornish et al., 1976) in which no relaxation in the obsesrved photocurrent was effected after heating the crystal to remove the remanent polarization by temporarily increasing the conductivity and cooling with and without a short circuit, nor by results (Glass et al., 1974) in which long periods of illumination resulted in no detectable decrease in the photocurrent as would be expected by the effects of photoconductivity.

iv) Bulk Photovoltaic Effect. Reasoning that any built-in internal field would be eventually relaxed by photoconductivity over long periods of illumination (which is not observed), Glass et al. (1974, 1975 a) were led to postulate the existence of a new transport mechanism, called the "bulk photovoltaic effect". The electrons which contribute to the photocurrent (and hence to the photorefractive effect) are trapped in asymmetric potential wells (the Fe^{2+} ions). Note in this regard that the Nb-Fe^{2+} distances in the $\pm$c-axis directions are different. Upon excitation, these electrons have a greater probability of moving along the +c-axis and therefore give rise to a net electron current J_{e1}. The displacement of the ionized impurity along the -c-axis due to Franck-Condon relaxation gives rise to a further current, J_{e2}. A third current, J_r, results from asymmetric retrapping of the excited elec-

tron by another ionized impurity (Fe^{3+}). The steady state photocurrent density, J_{ph}, can therefore be expressed as the sum

$$J_{ph} = J_{e1} + J_{e2} - J_r = \kappa\alpha I \tag{4.1}$$

where I is the incident light intensity, α is the absorption constant at that wavelength, and κ a constant (the "anisotropy constant") related to the physical nature of the trap. This model will be discussed in greater detail later.

5. PHOTOCURRENT AND BULK PHOTOVOLTAIC EFFECT

It has been noted (Chen 1969) that light incident upon poled ferroelectric single crystals causes a small current to flow between electrodes attached to opposite crystal faces without the application of an external field. Though initially thought to be caused by built-in fields due to, for instance, electric moments arising from cooling the crystal from a high temperature, subsequent experimentation has led to the conclusion that a new effect, the "bulk photovoltaic effect" is responsible.

i) Photocurrents

Figure 5-1 shows an example of a photocurrent caused by uniformly illuminating with an Argon-ion laser (514.5nm at 17.5 mW/cm^2) a face of an Fe doped $LiNbO_3$ crystal (perpendicular to the c-axis) and measuring the current passing between aluminum electrodes placed upon the c-faces. The transient component is the pyroelectric current caused by a change in the spontaneous dipole moment as the incident light raises the temperature. The opposite effect can be seen as the crystal cools after the light is turned off. The current component remaining after the pyroelectric current has become negligible is the photocurrent, which has the following properties:

a) the photocurrent strength is linearly related to the incident beam intensity and also depends upon wavelength (Cornish, 1975);

b) it does not change over long periods of time under constant illumination (10^2 hours or more);

c) it does not depend upon the thermal history of the crystal (i.e. the effect is not changed by heating and cooling the crystal under either open or short circuit conditions.

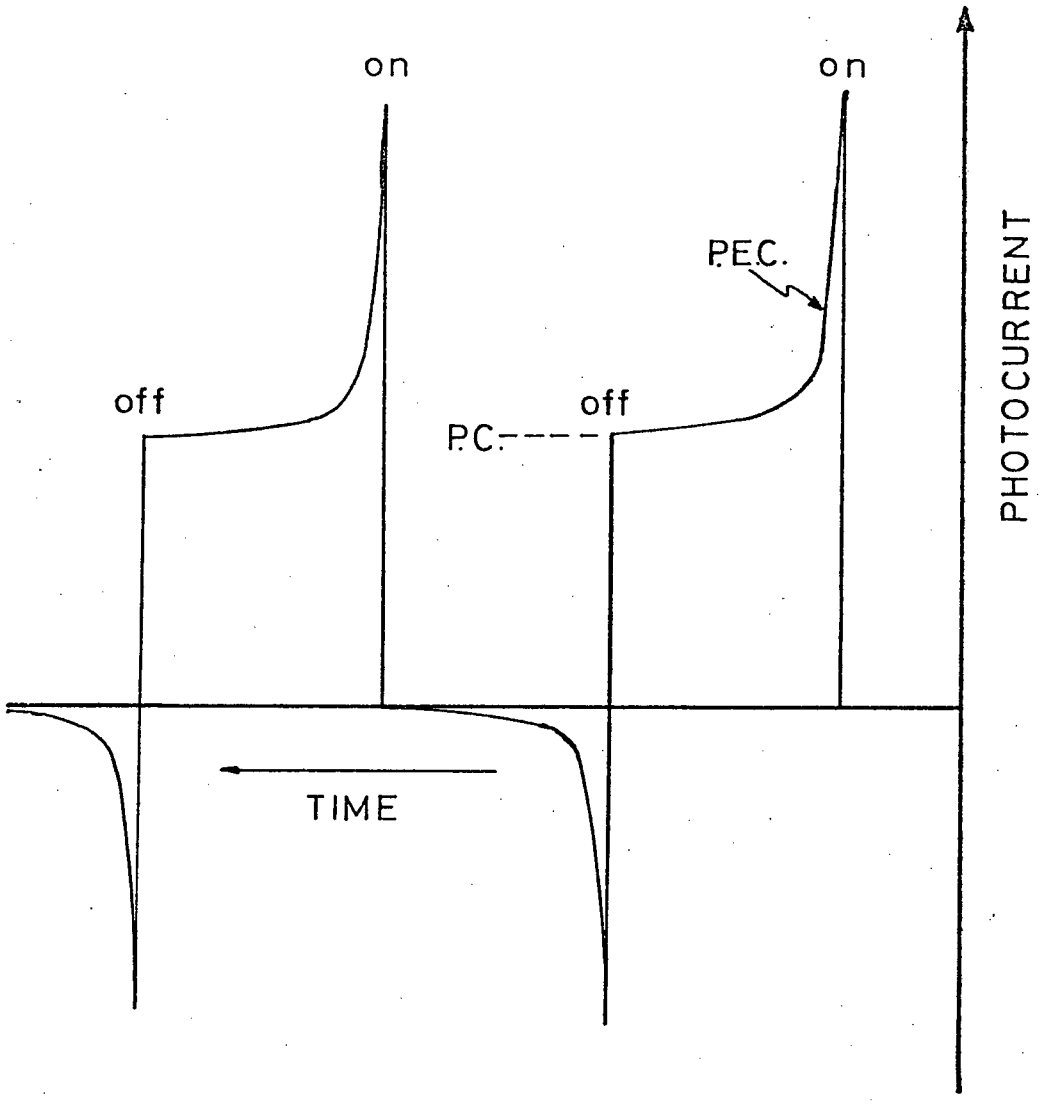

FIGURE 5.1

Graph of the pyroelectric current (PEC) and the photoelectric current (PC) which results when an expanded laser beam is directed at a $LiNbO_3$ crystal. The current is measured across the c-axis (see text).

A simple mathematical expression for the photocurrent density (Glass et al., 1974 b) is given by

$$J_{ph} = \kappa\alpha I \qquad (5.1)$$

where I is the incident beam intensity,

α is the absorption, and

κ is the photocurrent constant, which is dependent upon the nature of the crystal (impurities, defects, etc.).

ii) The Bulk Photovoltaic Effect

The observation of steady-state, short-circuit photovoltaic currents in regular crystals containing no macroscopic electric fields, concentration gradients or pn-like junctions led to a search for some bulk property of a crystal which could account for such an unexpected anisotropic effect. The several mechanisms proposed, which are not mutually exclusive, are briefly outlined here.

The asymmetric photo-delocalization model (Glass et al., 1974) centres on the fact that a $LiNbO_3$:Fe crystal has a unique polar axis along which the Fe-Nb distances are different in the +c and -c directions (see Appendix A). Consequently, there is a larger overlap between the orbitals of the Fe^{2+} ion with the Nb ion in the +c direction than those in the -c direction, which results in a preferred direction of transfer of electrons following optical excitation. This gives rise to a current, J_{el}, given by

$$J_{el} = q\xi \frac{\alpha I}{h\omega} \left(P_+ \ell_+ - P_- \ell_-\right) \qquad (5.2)$$

where ξ is the quantum efficiency,

$h\omega$ is the quantum of light energy,

P_+, P_- are probabilities of charge transfer in the +c and -c directions,

ℓ_+, ℓ_- are the electron mean free paths along these directions.

This is followed by Franck-Condon relaxation of the ions, with their net displacement along the polar axis giving a further current, J_{e2},

$$J_{e2} = \xi\left(\frac{\alpha I}{h\omega}\right) z_i \Delta\ell_i \quad \text{product summed over all i} \tag{5.3}$$

where $\Delta\ell_i$ is the displacement of the i^{th} ion,

z_i is the charge of the i^{th} ion.

Upon successive scattering, the motion of the photo-liberated electrons becomes random and they no longer contribute to a net current in the absence of an applied field. However, if the probability of a subsequent recombination at an impurity is dependent upon the direction from which the electron arrives, then we have a recombination current, as follows:

$$J_{r1} = \frac{q\xi}{h\omega}\left(\ell'_+ p'_+ - \ell'_- p'_-\right) \tag{5.4}$$

and another Franck-Condon relaxation current

$$J_{r2} = -\xi\left(\frac{\alpha I}{h\omega}\right) z'_i \Delta\ell_i \tag{5.5}$$

where the primed quantities ℓ'_+, p'_+, ℓ'_-, p'_- and z'_i in the recombination terms are analogous to the excitation quantities.

If we sum all of these currents we get

$$J_{ph} = J_{\varepsilon_{1,2}} + J_{r_{1,2}} = \kappa\alpha I \tag{5.6}$$

where

$$\kappa = \frac{q\xi}{h\omega}\left[\ell_+ p_+ - \ell_- p_- + \ell'_+ p'_+ - \ell'_- p'_-\right] + \frac{\xi\Delta\ell i}{h\omega}\left[z_i - z'_i\right]$$

and varies with the photon energy and environment of the absorbing centre. See Figure 5.2.

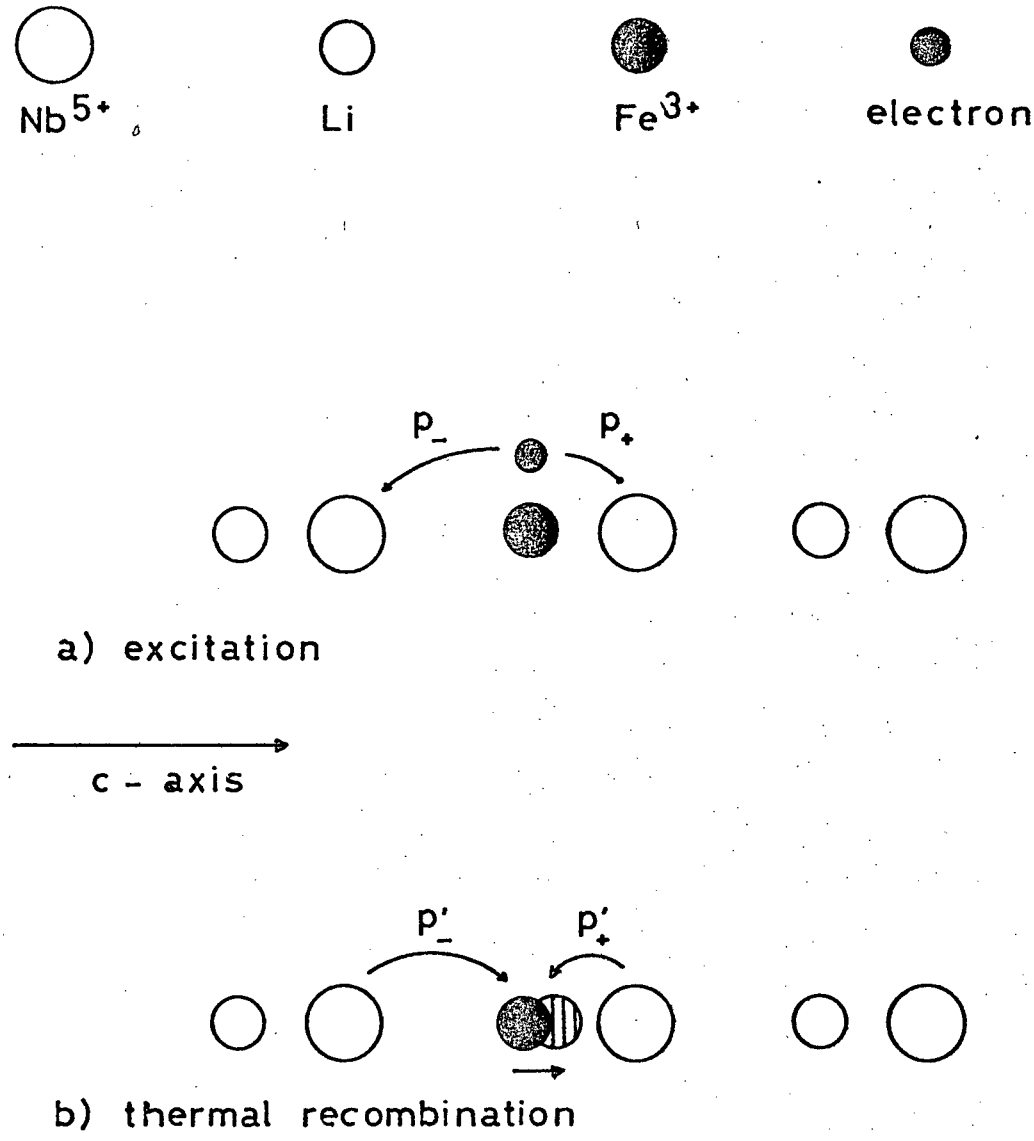

FIGURE 5.2

Asymmetric photo-delocalization model in a $LiNbO_3$ crystal. In (a) an electron is photoexcited from an Fe^{3+} impurity and has probabilities of p_+ and p_- of moving along the +c and -c axis directions respectively. In (b) is shown the Franck-Condon shift and electron recombination probabilities.

Whereas the above model involves electron transport between impurity ions, the photorefractive effect has been observed (von der Linde et al., 1974, 1975 a, 1975 b, 1976 and Ohmori et al., 1977) in high purity crystals as well.

The Collective Franck-Condon Relaxation Model attributes this to Franck-Condon relaxation of excited states following optical excitation. The physical mechanism of the model is shown in Figure 5.3a, where an anion and cation constitute a unit cell, and arrows represent the "direction of motion" to the next state. The ground state (i) is transferred to the Franck-Condon state (ii) by optical excitation. The cation then shifts a distance Δx to the relaxed excited state (iii) according to the coordinate configuration diagram (Figure 5.3b). Up to this point there has been both a directional electronic charge transfer current, J_{ee}, and an ionic relaxation current, J_{ie}. Next the cell goes to the ground Franck-Condon state (iv) as the electron retreats to the anion and then to the ground state (v) as the cation assumes its original location in the lattice. These motions contribute electronic and ionic relaxation currents, J_{er} and J_{ir}, which cancel out the previous two currents if the electron and cation return to their original locations. However, if the electron ends up combining with an anion in a neighbouring cell as shown in (v), a non-zero contribution to the net current results. Furthermore, if coherent relaxation of the lattice involving a nonisotropic recombination probability (recombination to the right in (v), for instance) is present, the summed effect will be a bulk steady-state photocurrent.

A third model is the Photofluctuation Model (Fridkin, 1977), which attributes the BPE in some oxygen octahedra ferroelectrics (i.e., $BaTiO_3$, $LiNbO_3$) to photoinduced polarization fluctuations. Light absorption in n-type ferroelectric crystals results in the production of free and trapped electrons. A trapped electron can interact with an optical phonon to create a photoinduced fluctuation of polarization localized near the trap (Chanussot, 1974). Within

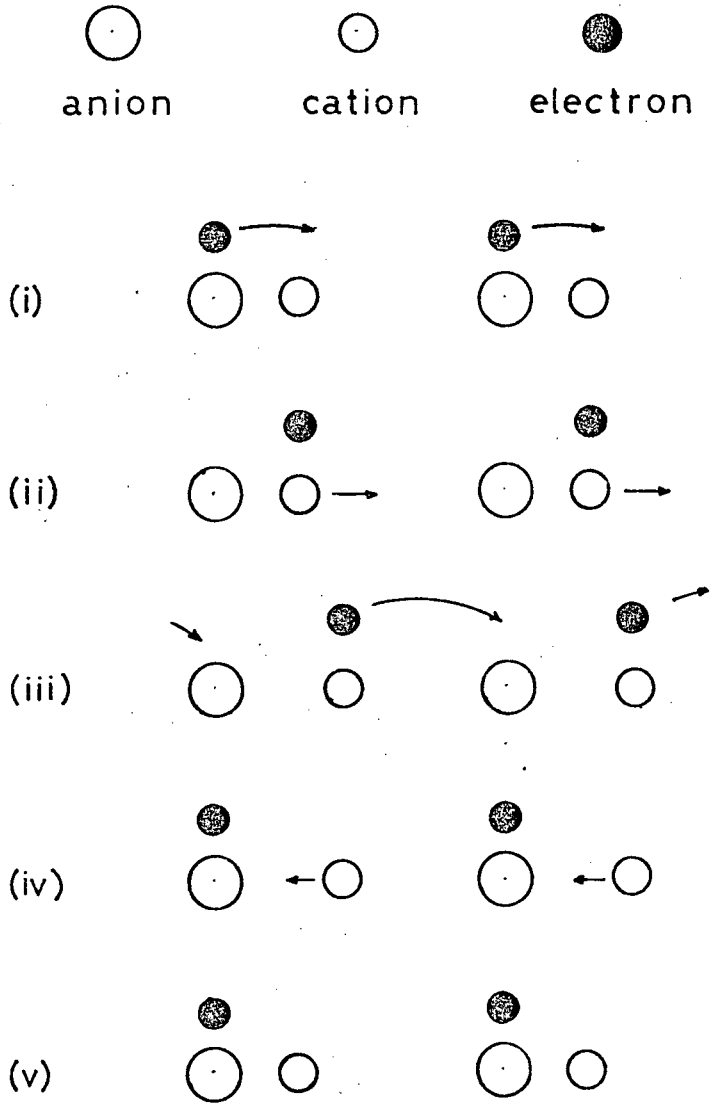

FIGURE 5.3a

Physical mechanism of the collective Franck-Condon relaxation model showing in successive time frames: (i) photo-excitation from the ground state to an excited Franck-Condon state; (ii) cation shift to the "relaxed excited state"; (iii) electron transfer leading to the ground Franck-Condon state; (iv) cation shift to the ground state.

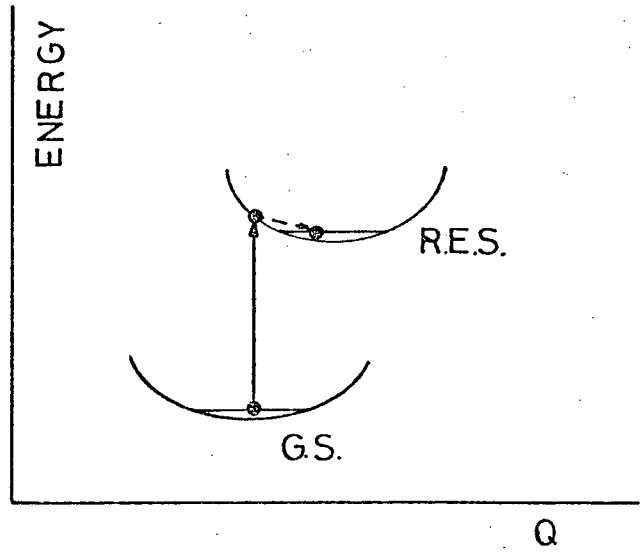

FIGURE 5.3b

Coordinate configuration diagram for the Franck-Condon model showing the first two events described above.

the volume of the fluctuation there occurs a change in spontaneous polarization, ΔP, which gives rise to an electric field $\Delta E \approx \Delta P/E$. Symmetry requires that all photoinduced fluctuations be in the same direction. A bulk photovoltaic effect results from the free photo-excited electrons coupling to these fluctuations and moving in the direction of ΔE. This model suggests that additional Rayleigh scattering of light should be present, and this has been observed in $BaTiO_3$, though not in $LiNbO_3$ (Chanussot et al., 1977).

The Polarized Impurities Model (von Baltz, 1977) assumes that the randomly distributed ground state impurities which provide photoconduction electrons are polarized due to an asymmetric short-range potential. The photocurrent then arises from an asymmetry in the photo cross-section for ionization from the ground state to a delocalized final state, $s(\Omega) \neq s(-\Omega)$, where $s(\Omega)$ is a photo-ionization cross-section resulting in the ejection of an electron in a direction Ω. The photocurrent density is given by

$$J_{ph} = \kappa\alpha I = \frac{q\xi I\alpha L_p}{h\omega} \tag{5.7}$$

where N is the impurity concentration,

L_p is the electron transport length due to the photovoltaic effect, and

$$\alpha = N \int s(\Omega)\, d^2\Omega \tag{5.8}$$

This model provides an explanation for the different spectral properties of the photovoltaic current for light polarized parallel and perpendicular to the direction of spontaneous polarization, and for observed changes of sign of the current, as in $BaTiO_3$ (Koch et al., 1976). Also, it does not predict the generation of a macroscopic dark current due to thermal excitation which, though not obsesrved, is predicted by the asymmetric photodelocalization model.

Early studies of the bulk photovoltaic effect led to the following

expression relating photocurrent density, J_{ph}, to incident light intensity, I:

$$J_{ph}(x) = \kappa\alpha I(x) \tag{5.9}$$

However, more recent work (Young et al., 1979) has pointed out that this simple expression predicts neither beam coupling during hologram writing nor a dependence of the recording material response upon the spatial frequency of the incident light. Both of these are observed characteristics of holograms written in ferroelectric crystals. As will be discussed later, the beam coupling during writing is a result of a phase shift between the holographic grating being written and the diffraction pattern writing it. Also, the "ac" part of the current is smaller for fringes with higher spatial frequencies.

The search for a more realistic expression for the photovoltaic current starts with the choice of a set of assumptions concerning the microscopic mechanisms involved. The first assumption is that photoelectrons are preferentially ejected along the direction of the +c-axis. It then follows that we can define a quantity, L_p, which is the mean distance travelled by the electron before being retrapped or having its motion randomized. The second assumption deals with the manner of trapping. Young et al. dealt with three possibilities:

a) continuous scattering - closely spaced scattering centres along the c-axis gradually randomize the direction of motion of the photo-liberated electrons,

b) fixed transport length - the photo-liberated electrons travel a fixed distance, L_p, along the +c-axis and are then trapped or have their motion randomized at that point,

c) discrete scattering - identical scattering centres spaced L_p apart along the c-axis and each having a probability $p'<1$ of scattering the electron and probability $p = 1-p'$ of not affecting its motion.

Once the second assumption is decided upon, the construction of a mathematical model for the photocurrent involves finding an expression for the photocurrent density light impulse response and then forming the convolution of this with the appropriate incident light pattern, in this case a sinusoidally varying grating in the +c-axis direction:

$$I(x) = I_o (1 + \cos Kx) \tag{5.10}$$

The results of these calculations give (Young et al. 1979), for the three cases:

a) continuous scattering

$$J_p(x) = -\kappa\alpha I_o \left[1 + m' \cos (Kx-\phi_p)\right] \tag{5.11a}$$

where

$$K = \frac{\xi a L_p}{h\omega}$$

$$m' = m\left[1 + (KL_p)^2\right]^{-1/2}$$

$$\phi_p = \tan^{-1} (KL_p)$$

b) fixed transport length

$$J_p(x) = -\kappa\alpha I_o \left[1 + m' \cos (Kx-\phi_\ell)\right] \tag{5.11b}$$

where

$$\kappa = \frac{\xi a L_p}{h\omega}$$

$$m' = m \operatorname{sinc}\left[\frac{KL_p}{2\pi}\right] \quad ; \quad \operatorname{sinc}(x) = \frac{\sin \pi x}{\pi x}$$

$$\phi_p = \tan^{-1}\left[\frac{KL_p}{2}\right]$$

c) discrete scattering centres

$$J_p(x) = -\kappa\alpha I_o\left[1 = m' \cos\left(Kx-\phi_p\right)\right] \qquad (5.11c)$$

where

$$\kappa = \frac{q\xi L_p}{p'h\omega}$$

$$m' = mp\ \mathrm{sinc}\left[\frac{KL_p}{2\pi}\right]\left(1 + p^2 - 2p\cos KL_p\right)^{1/2}$$

$$\phi_p = \frac{KL_p}{2} + \tan^{-1}\left[\frac{p \sin KL_p}{1 - p\cos KL_p}\right]$$

Note that in all three cases, I(x) in eq. 5.9 has been replaced by I_o plus a spatially varying (ac) component which is phase shifted by an amount ϕ_p. In all three cases the anisotropy constant, κ, which gives the strength of the bulk photovoltaic effect, varies linearly with L_p. Also, the phase shift ϕ_p is such that it goes to zero as L_p goes to zero. The functional dependence of m' upon the spatial frequency of the fringe pattern, K, shows that high spatial frequencies result in a smaller "ac" current and thus less efficient hologram writing.

It should be pointed out that it is quite possible that some weighted combination of all three of these cases (and possibly others) may be applicable to hologram formation in a real crystal, and thus detailed numerical work may not reveal one of them to be clearly and solely responsible for the grating formation. However, they all agree on several important points, and thus provide a useful starting point for experimental analysis.

6. HOLOGRAM WRITING IN $LiNbO_3$ CRYSTALS

Having considered beam coupling in an "ideal" thick phase grating in Chapter 3, and the basic processes involved in writing a hologram in Chapters 4 and 5, we now consider the theory of hologram writing in $LiNbO_3$.

In the first treatments of this problem (e.g. Staebler and Amodei, 1972) neither the feedback effect of the rising space charge nor the effect of self diffraction of the writing beams on the hologram grating were taken into account. Also, the conclusions concerning the relative phase between the FP and HG rested on an implicit, though unrealized, assumption of short transport length of the migrating electron. It was shown that if diffusion was the main means of electron transport, the hologram grating is shifted by $\pi/2$ with respect to the fringe pattern. If drift is the only means of electron transport there is no phase shift (and consequently no energy transfer). Later work (Young et al., 1979) showed that if the drift transport length is not much less than the fringe spacing then some phase shift is observed, and as the drift length approaches or exceeds the fringe spacing, one obtains also the $\pi/2$ shifted HG at the initial stage of recording. This analysis was applicable only to thin layers of optical crystals or to the initial stages of recording when energy and phase redistribution between the two beams may be neglected.

Shortly afterwards, a dynamic theory of hologram recording was put forward (Ninomiya, 1973) based upon the solution of nonlinear wave equations with the dielectric constant dependent upon the light intensity. Whereas this and several succeeding papers used a postulated dependence of refractive index upon intensity, Kukhtarev et al. (1979) derived it from the material equations. Though their theory includes the photovoltaic current, their subsequent experiments were conducted on crystals and under conditions where the effects of

diffusion dominate, and thus do not confirm the accuracy of their predictions vis-a-vis the BPE.

The theoretical development given here follows Moharam et al. (1979) and will be applied to the initial stages of hologram formation before the effects of feedback and self-diffraction become significant. The following conditions and assumptions hold:

i) arbitrary electron transport length,

ii) external short on crystal,

iii) uniform illumination of crystal with geometry as in Figure 6.1.

The expression for the fringe pattern formed by the two interfering beams is:

$$I(x) = I_o (1 + m \cos kx) \tag{6.1}$$

where

$m = 1$ (modulation ratio for $I_R = I_S$),

$k = 4\pi \sin \theta/\lambda$ (fringe pattern wave vector).

The conduction current density distribution along the x-axis is

$$J(x) = qD \frac{\partial \rho(x,t)}{\partial x} + q\mu\rho(x,t)E_{sc}(x,t) + J_p(x,t) \tag{6.2}$$

with the three terms representing diffusion, drift (due to the photo-induced space charge field $E_{sc}(x,t)$), and the BPE. The free electron concentration is the sum of the dark concentration and photoexcited concentration:

$$\rho(x,t) = \rho_D + \rho_L(x,t) \tag{6.3}$$

Reasoning that for uniform illumination, the photovoltaic current density equation should reduce to the expression obtained by Glass et al. (1974 b) (see eq. 5.1), Young et al. (1979) put forward the following expression (see eq. 5.11):

$$J_p(x) = -\kappa\alpha I_o\left[1 + m f_1\,(k,L_p)\cos\,(kx-\phi_p)\right] \tag{6.4}$$

where $0 \leq f_1\,(k,L_p) \leq 1$ is a real function which can be set equal to unity for our purposes. They also pointed out that if the photovoltaic transport length is not small with respect to the fringe spacing, then the $\kappa\alpha I$ term is not strictly correct. The photoexcited electron concentration in eq. 6.3 follows from

$$0 = \frac{\partial \rho_L(x,t)}{\partial t} = g(x) - \frac{\rho_L(x,t)}{\tau} + \frac{1}{q}\frac{\partial J(x,t)}{\partial x} \tag{6.5}$$

where $g(x)$ is the volume generation rate,

$$g(x) = g_o\left[1 + m\, f_2\,(k,L_p)\cos\,(kx-\phi_p)\right] \tag{6.6}$$

and $\partial\rho_L(x,t)/\partial t \approx 0$ constitutes an assumption that the photoexcited electron concentration is time invariant for steady illumination. We combine eq. 6.6 with the continuity equation for trapped charge density, ρ_{sc}, due to carrier migration

$$\frac{\partial \rho_{sc}}{\partial t} = -\frac{\partial J(x,t)}{\partial x} \tag{6.7}$$

and with Poisson's equation

$$\frac{\partial\, E_{sc}(x,t)}{\partial x} = \frac{\rho_{sc}}{\varepsilon} \tag{6.8}$$

to get (after integrating over space and time)

$$E_{sc}(x,t) = -\frac{1}{\varepsilon}\int_o^t J(s,t)\,dt + A(t) \quad . \tag{6.9}$$

The constant of integration comes from the assumption (ii above) that there is a short across the crystal,

$$\int_o^L E_{sc}(x,t)\,dx = 0 \tag{6.10}$$

from which we get

$$E_{sc}(x,t) = -\frac{1}{\varepsilon}\int_{o}^{t}\left[J(x,t) - J_o(x,t)\right]dt \quad . \tag{6.11}$$

Here, J_o is the average conduction current density. Solving the above we can derive [Moharam et al. (1979), El Guibaly (1979)] an expression for the space charge field:

$$E_{sc}(x,t) = \frac{qg_o tm}{\varepsilon k}\,\frac{\left[(kL_p)^2 + (kL_d)^4\right]^{1/2}}{1 + (kL_d)^2}\cos\,(kx-\phi_p-\phi_d) \tag{6.12}$$

(for the case of large scale drift), where

$$\phi_d = \tan^{-1}\frac{(kL_d)^2}{kL_p} = \tan^{-1}\frac{E_D}{E_V}$$

$$E_D = k_B\frac{kT'}{q} \qquad T' = \text{absolute temperature},\quad k_B = \text{Boltzman's const.}$$

$$E_V = \frac{L_p}{\mu\tau} \qquad \text{is the virtual field} \quad .$$

$$L_d = (\tau D)^{1/2} \qquad \text{diffusion transport length} \quad .$$

ϕ is the phase shift due to the finite photovoltaic transport length.

Knowing the distribution for the space charge field we can find the refractive index distribution which constitutes the grating (see Appendix A), and then use the results of Chapter 4 to relate this to the beam coupling.

7. APPARATUS

Figure 7-1 is a schematic of the entire experimental setup used in this study. All optical components including the laser were placed on a massive cement bench for mechanical isolation from building vibrations, and metal strips were cemented to the top surface to provide a surface for magnetic component stands. Slamming doors and rolling carts down the hall still had an effect on the readings so most experimentation was done in the evening. The light source was a Spectra Physics Model 166 argon-ion laser operated CW at 514.5nm, at which it has a maximum specified output power of 800mW (for TEM_{00} mode), though only 515mW was obtained. It was generally operated for 30 minutes before runs to allow it to reach a stable output power.

The beam was directed by mirror M1 into a plexiglas and aluminum "greenhouse" which served to isolate it from thermal air currents which cause random fluctuations in the phase path length. Those parts of the beam path where the beam was separated and then brought together to form an interference pattern were further isolated from air currents by being enclosed in paper tubes for most of their length.

A small fraction of the beam was split off by BS_1 before the hologram setup and used in a Michelson interferometer (BS_2, M_2, M_3, M_4, screen) for the purpose of forming an interference pattern of visible dimensions. This allowed simultaneous visual monitoring of bench vibrations, which was useful in diagnosing occasional problems experienced in forming holograms.

The main portion of the beam continued on through a spatial filter to a collimating lens positioned at slightly more than its focal length from the filter pinhole so that the beam converged to a point at the beam splitter BS_3 half way between the lens and crystal. This was done for two reasons:

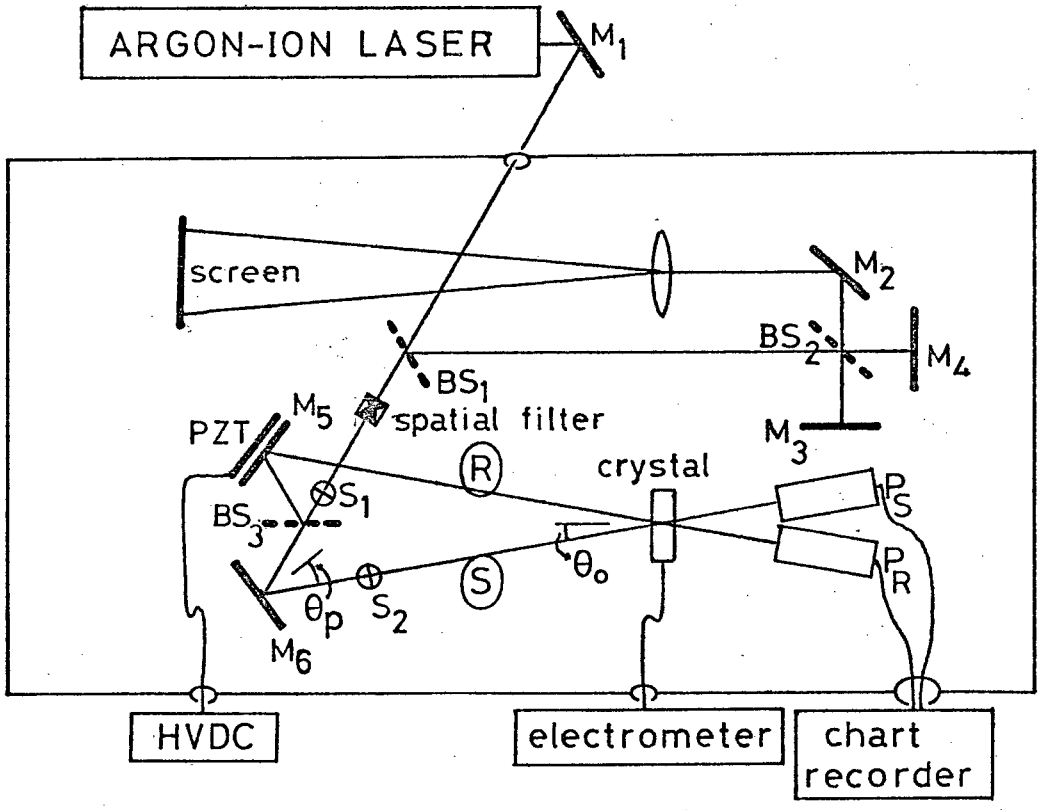

FIGURE 7.1 (experimental apparatus)

The laser beam is directed into the plexiglass "greenhouse" by mirror M_1. Beam splitter BS_1 diverts a portion of the beam for use in a Michelson interferometer (BS_2, M_3, M_4, M_2, lens screen) to provide a macroscopic diffraction pattern on the screen to monitor bench vibration. The rest of the beam passes through a spatial filter and collimating lens, past a shutter S_1 to the beam splitter BS_3. Then two beams of equal intensity are reflected from M_5 and M_6 towards the crystal where they come together to form a fringe pattern. The intensities of the coupled beams transmitted by the crystal are monitored by the photometers P_S and P_R. The fringe pattern at the crystal can be shifted parallel to the crystal c-axis by adjusting the voltage on the piezoelectric disc upon which mirror M_5 is mounted. Opening shutters S_1 and S_2 causes both beams to pass (writing), whereas opening only shutter S_1 lets only the reference beam through (reading/erasing). The beams between the mirrors M_5 and M_6 and the crystal are enclosed in paper tubes to further reduce air current problems.

i) it permitted the insertion of small apertures in both beam paths immediately after splitting by BS_3 in order to block off secondary beams arising from internal reflection in the splitter, which interfered with the main beams;

ii) the continuously variable beam splitter gives a more nearly uniform amplitude in the two resulting beams if the incident beam has a small cross section.

Thin geometry was adopted in preference to one in which two spatial filters were placed after BS_3 to avoid having to spend too much time tuning the filters in order to balance beam intensities at the crystal. The resulting beam divergence of the new geometry (< 20 mR) did not seriously affect the assumption of interfering plane waves.

After being split, the beams are reflected from mirrors M_5 and M_6 towards a point where they intersect, forming a diffraction pattern of vertical planes in the crystal held in the crystal holder. One of the two mirrors is mounted on a PZT ceramic disc, thus providing the capability to electrically vary one of the phase path lengths with respect to the other.

The beam intensities emerging from the crystal are then monitored by two silicon p-n junction photodetectors, one an Alphametrics Model Pl110S driving a Model DC1010 display, and the other a model PS1101S driving a Model 1030 display.

A Keithley 602 electrometer was connected across the crystal faces perpendicular to the c-axis to measure the photocurrent.

The PZT disc was driven by a Fluke Model 405B high voltage power supply, which is discretely variable in 0.1V steps within a ±3000V range.

A Moseley Autograf Model 7100 BM two channel strip chart recorder was used to monitor any two of the four relevant parameters: PZT voltage (through a 10:1 voltage divider), electrometer output and the two photodetectors.

A DC voltage supply was used to drive the two shutters S_1 and S_2, which allowed either both beams (writing), the reference beam (reading) or neither beam to reach the crystal.

Lastly, to erase the holograms, the crystal was short circuited across the c-faces with a platinum wire mesh to prevent damage from stresses of pyroelectric origin, and placed in a holder which was placed in an aluminum box to ensure even and gradual heating and cooling in the oven.

8. MEASUREMENTS AND ANALYSIS

8.1 Measurements

In the following we make the assumption of a lossless dielectric by setting $I_R(z=0) + I_s(z=0) = I_R(z=d) + I_s(z=d)$. The diffraction efficiency is then calculated from measurements when $I_s(z=0)$ as

$$\eta = \frac{I_s(z=d)}{I_s(z=d) + I_R(z=d)} \tag{8.1}$$

The amount of coupling, C_R and C_s, between the two beams when $I_R(z=0) = I_s(z=0)$ results in normalized values of

$$C_s = \frac{I_s(z=d)}{\left[I_s(z=d) + I_R(z=d)\right]/2} \quad \text{and} \quad C_R = \frac{I_R(z=d)}{\left[I_s(z=d) + I_R(z=d)\right]/2} \tag{8.2}$$

The crystal used (#6 - see Appendix A) was 0.1 mole percent iron doped and antireflection coated to reduce complications in the fringe pattern due to internal reflection.

Fig. 8.2 is a photocopy of strip chart recorder output (1.25 cm/min) of a pair of photodetectors monitoring the intensities of the transmitted subject and reference beams, $I_s(z=d)$ and $I_R(z=d)$ as a hologram is recorded The following features are present:

i) Lines 'C' and 'D' are the transmitted subject and reference beam intensities respectively. These start out equal ($5mW/cm^2$) but their intensities diverge as time progresses due to beam coupling.

ii) At regular intervals the incident subject beam is interrupted by a solenoid operated shutter causing $I_s(z=d)$ to drop ('a' in figure) and $I_R(z=d)$ to remain unchanged. As the hologram develops, however, some of the reference beam is diffracted into the subject beam path and the intensity of $I_S(z=d)$ gradually increases (line

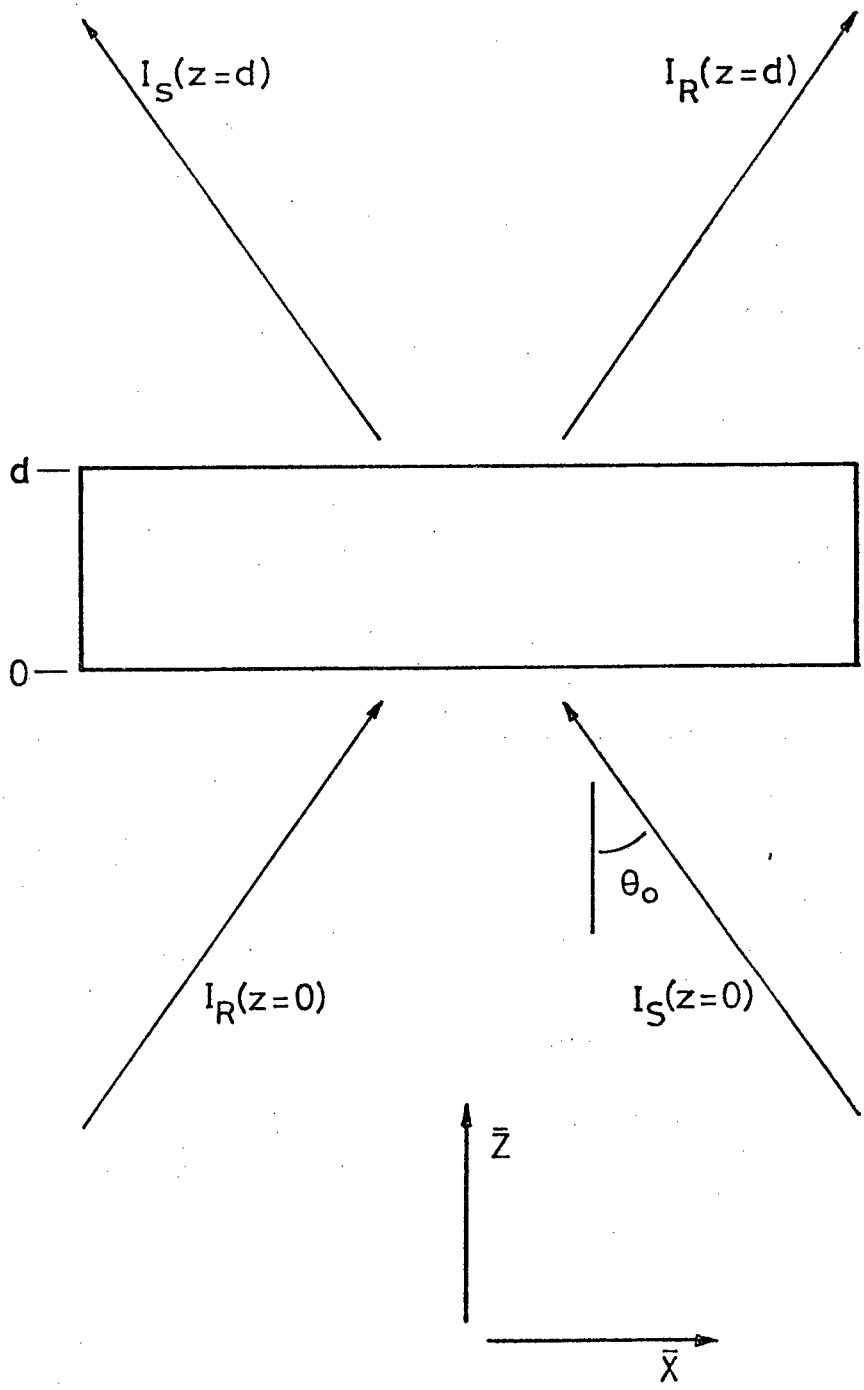

FIGURE 8.1

Beam geometry during hologram writing (eq. 8.1, 8.2).

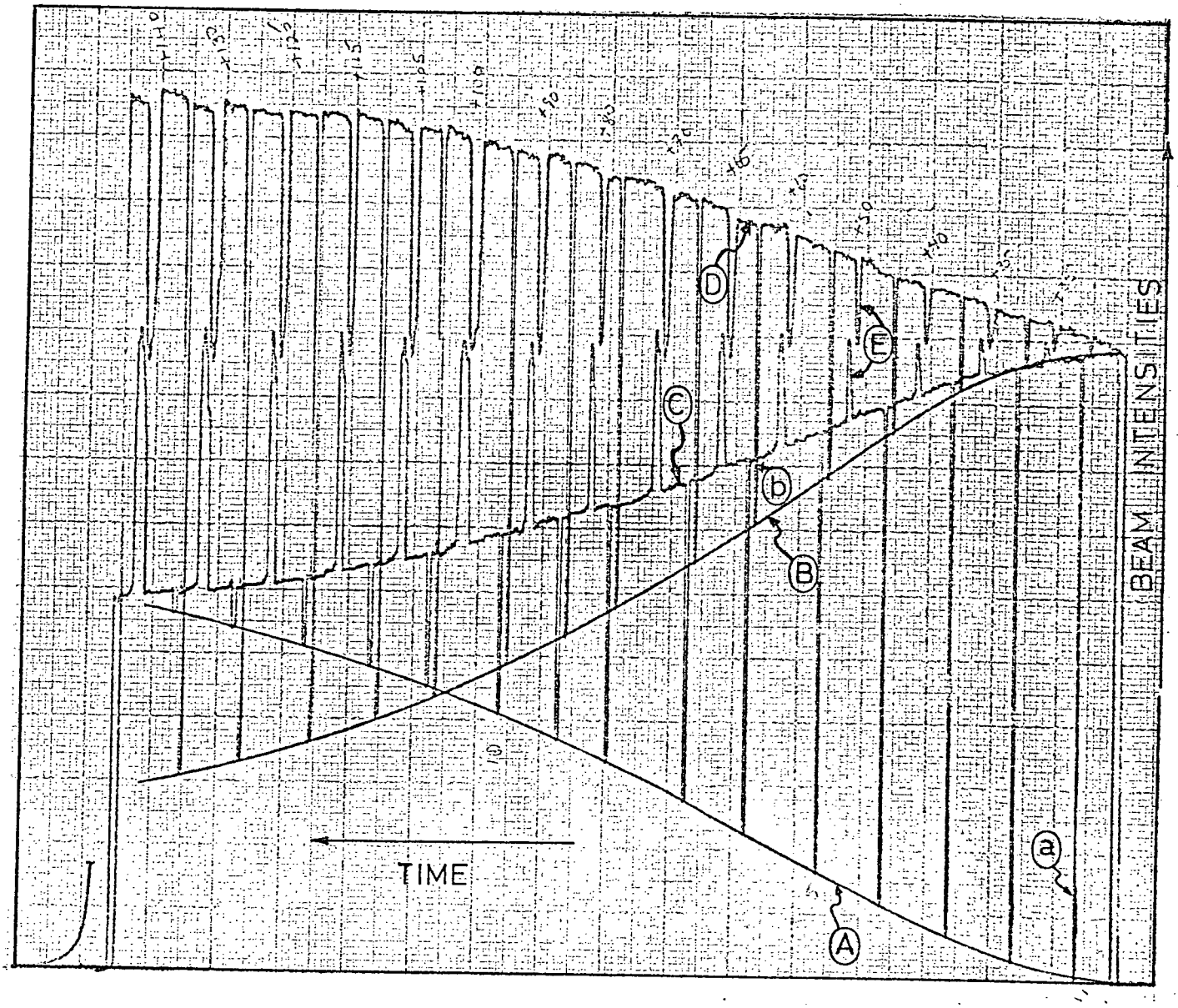

FIGURE 8.2

Development of hologram, showing:

i) beam coupling (C,D)

ii) diffraction efficiency for momentary reading (a,A,b,B)

iii) "nulling voltage" (E)

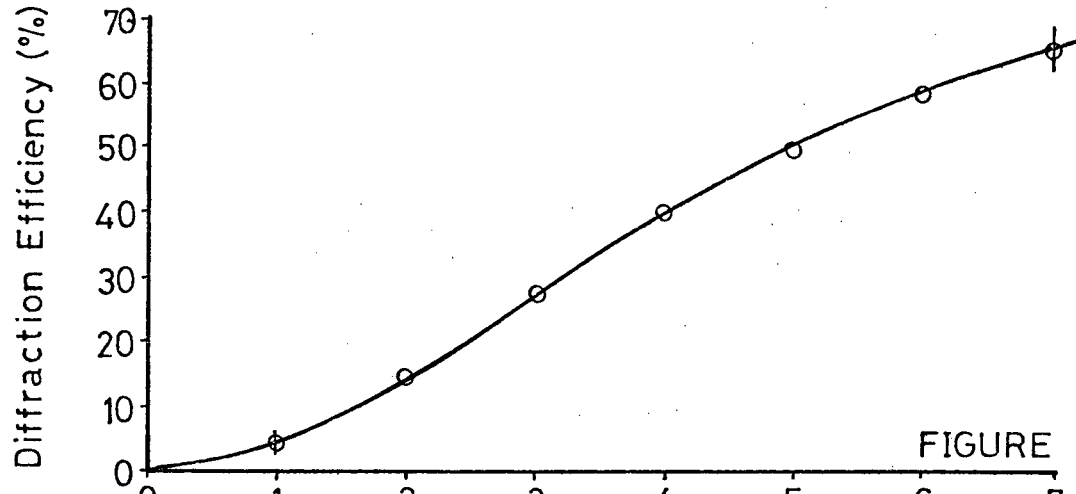

FIGURE 8.3a

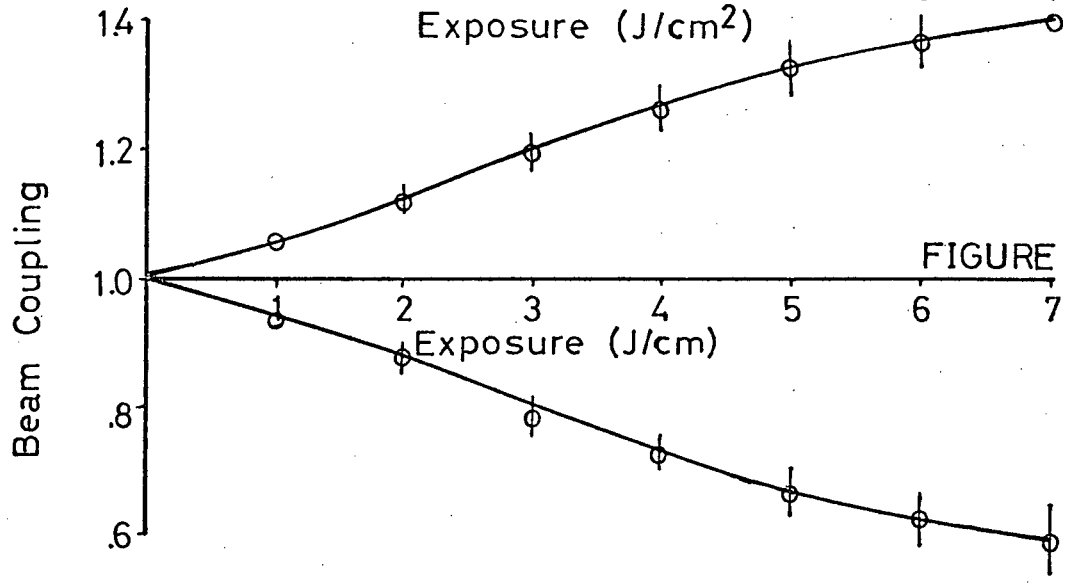

FIGURE 8.3b

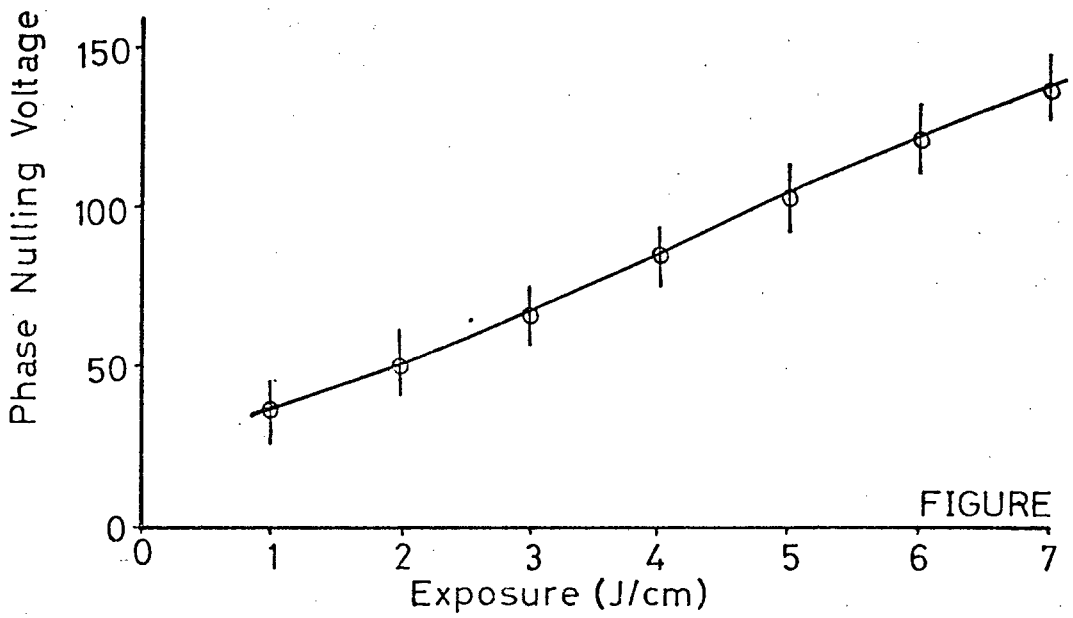

FIGURE 8.3c

'A') and that of $I_R(z=d)$ decreases (line 'B'). Points on lines 'A' and 'B' are inserted into equation 8.1 to obtain values for the diffraction efficiency as a function of time.

iii) Also, the intervals of the coupled beams were balanced at regular intervals $\left[I_R(z=d)\right.$ set equal to $\left.I_s(z=d)\right]$ by varying the spatial phase relationship ϕ between the fringe pattern and hologram grating. This was achieved by applying the appropriate voltage to the PZT disc (see Fig. 7.1), and is represented by the spikes 'E' on Fig. 8.2 with the corresponding voltages written above.

Figure 8.3a is a graph of the development of the normalized diffraction efficiency (eq. 8.1) from Fig. 8.2. The x-axis units are exposure (joules/cm^2) which can be calculated from the incident intensities $\left[I_s(z=0) = I_R(z=0) = 5.0\ \text{mW/cm}^2\right]$, the angles of incidence from the normal ($\theta_o = \pm 19°$) and the chart recorder speed (1.25 cm/min.). Figure 8.3b is a graph of the development of the amount of beam coupling (lines 'C' and 'D' in Fig. 8.2 normalized with equations 8.2). Figure 8.3c is a graph of the voltage required to null the coupling.

It was seen in Chapter 3 that a simple sinusoidal fringe pattern incident upon a simple sinusoidal holographic grating will result in beam coupling and a transfer of energy from one beam to the other (eq. 3.8) if there is a non-zero spatial phase ϕ between the fringes and grating (Fig. 3.1). (Here, "simple" means that there is no variation in either the fringe pattern or the grating in the Z direction.) Therefore, whether or not we are actually dealing with simple gratings and fringe patterns, an effective phase shift ϕ_e can be defined which is the shift which would account for the coupling if in fact simple fringes and gratings were present. ϕ_e can be obtained from the data in two ways:

i) direct calculation from the "nulling voltage" V:

$$\phi_e = \frac{V}{V_{2\pi}} \times 360 \text{ (degrees)}$$

where $V_{2\pi}$ = 1180 volts is the voltage which causes a full 2π phase shift, and is determined by the piezoelectric coefficient d_{22} of the phase shifter (Appendix B) and by the angle θ_p (Fig. 7.1), and

ii) calculations from the data in figures 8.3 a and b inserted into equations 3.8, 3.9 and 8.1.

These are plotted in Fig. 8.4 along with the results from two other experimental runs. The three features of note are that the variation in phase with exposure is approximately linear over the range of observation, that all lines have approximately the same intercept at Exp. = 0, and that the slopes of the lines vary not only with different sets of data but also with the means of calculation (i and ii above).

The coupling shown in Fig. 8.3b can be compared to that of Fig. 8.5, which shows that the development of coupling can be different for nominally identical experiments. However, it is possible to extract useful information from the coupling despite its irregular behaviour. This entails a closer examination of the reasons for the time variation of the calculated phase shifts.

8.2 Analysis of Phase Shift Measurements

Figure 8.4, which shows that the phase shift varies with time, demonstrates why graphs like Fig. 8.6 giving the predicted coupling for various constant values of the shift are not observed experimentally. There are several apparent reasons why the phase difference between the grating and fringe pattern varies as the hologram is written.

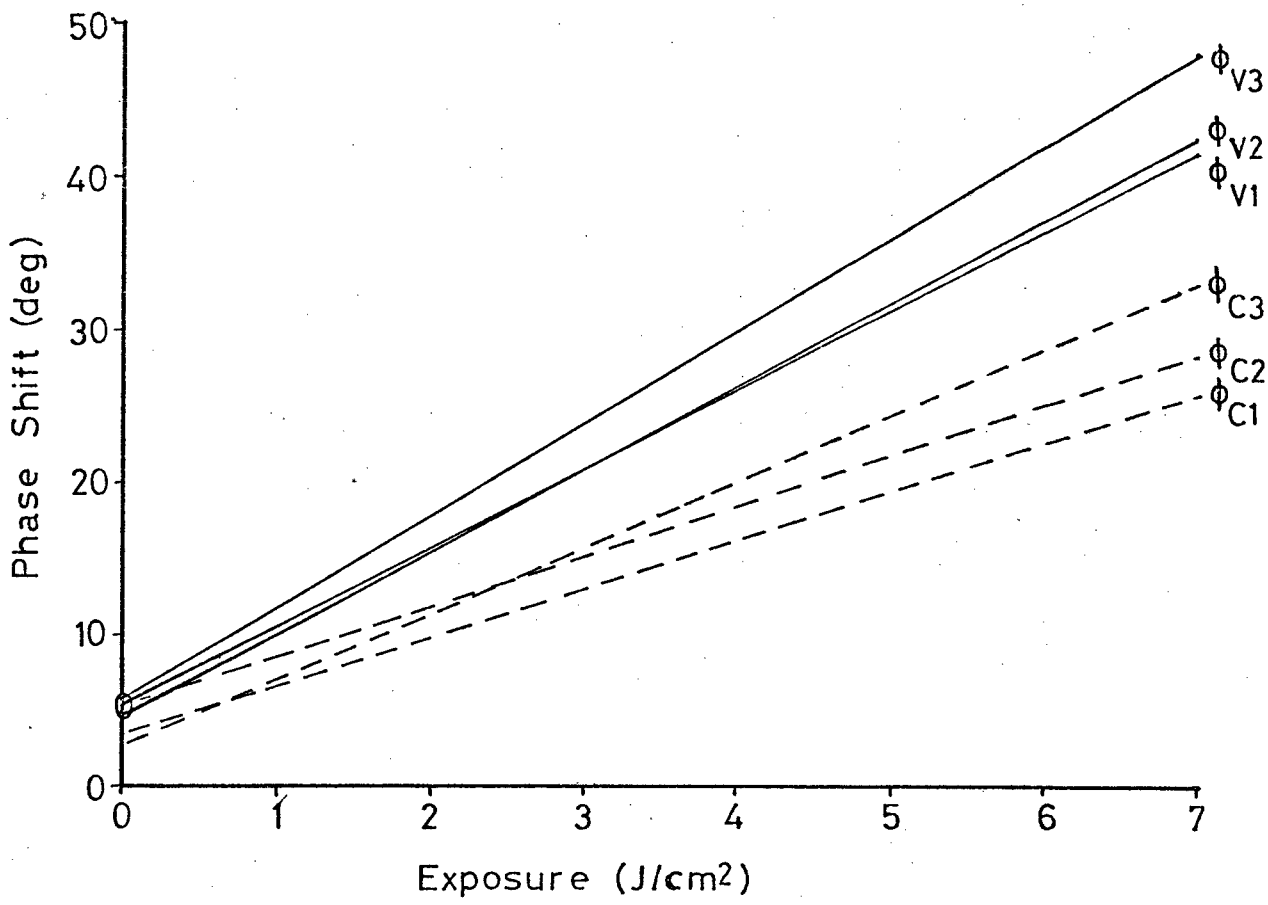

FIGURE 8.4

Variation of phase shift with exposure for three runs:

i) Dashed lines calculated using equations 3.8, 3.9, and the measured values for the diffraction efficiency and coupling.

ii) Solid lines calculated directly from nulling voltage of PZT shifter.

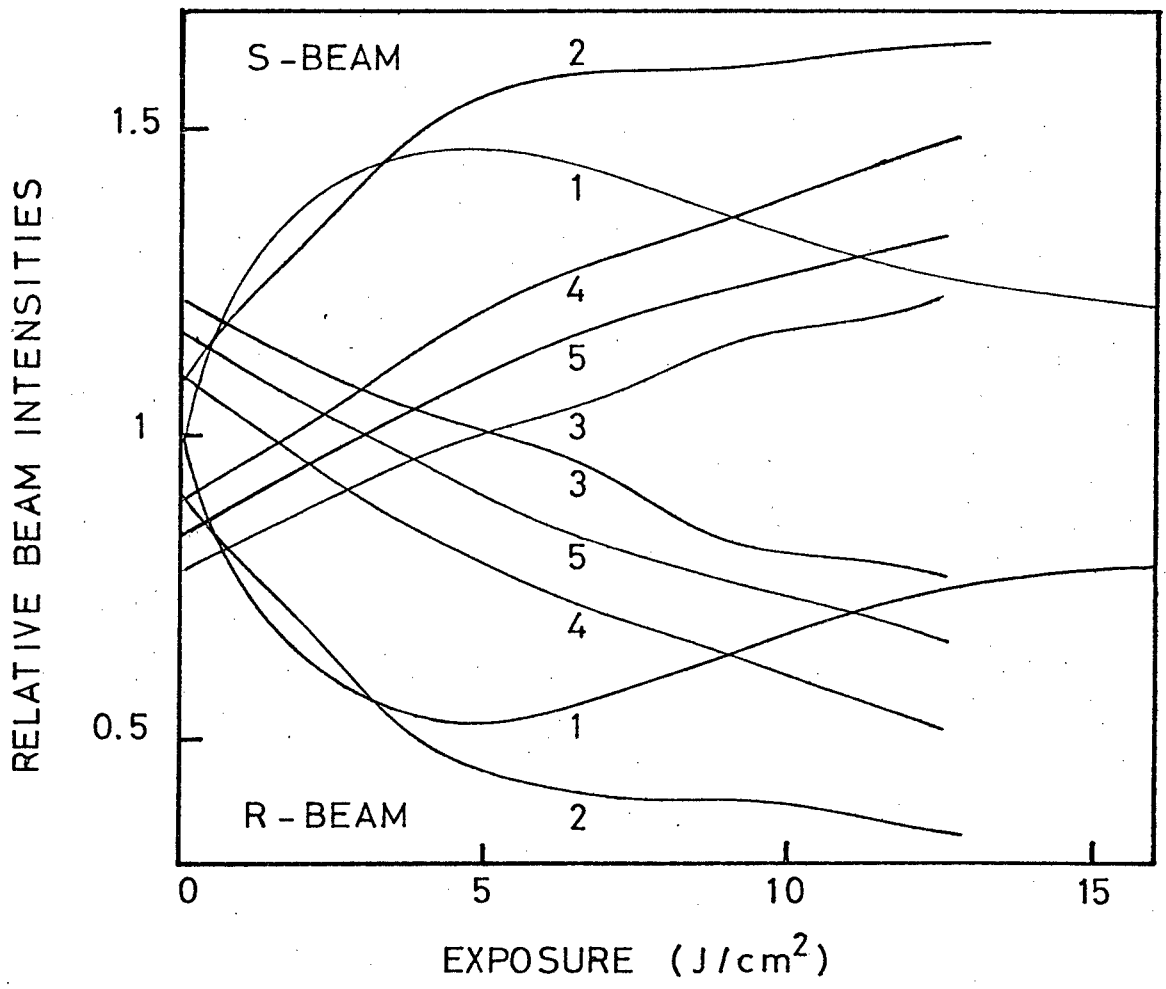

FIGURE 8.5

Time development of beam coupling for five nominally identical experiments. The beam intensities are normalized by dividing each by one-half their sum. From Young et al. (1979).

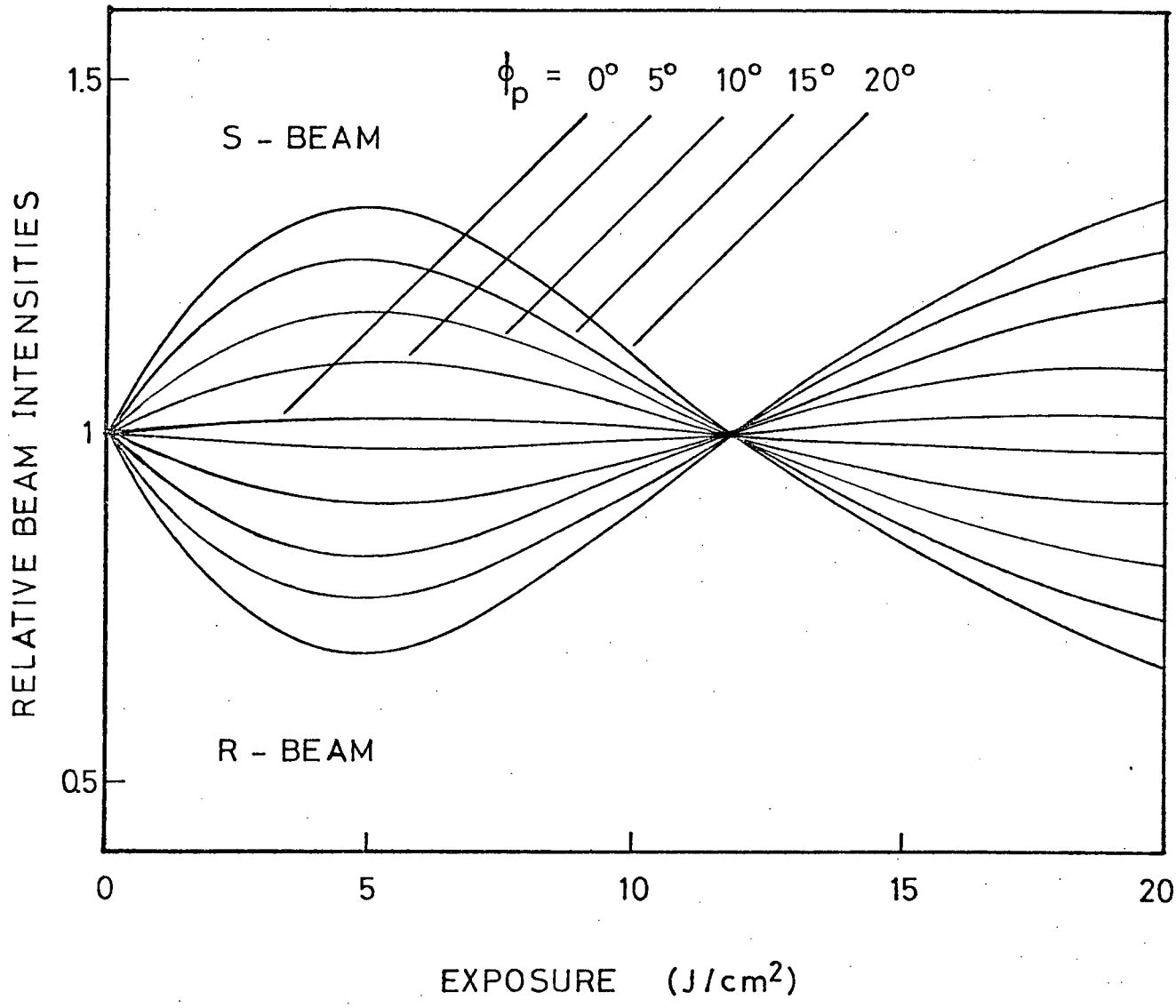

FIGURE 8.6

Beam intensities calculated from a computer model for different assumed values of the phase shift ϕ (constant) associated with the bulk photovoltaic effect. From el Guibaly (thesis).

8.2.1 Grating Bending

It has been shown (Staebler et al., 1972) that the phase of the hologram grating varies along the z-axis as time (exposure) increases. This is illustrated in Fig. 8.7, which uses data obtained from a program developed by Moharam (1978) and later modified by el Guibaly (1979) for the case of a crystal 1mm thick with an angle of incidence of 19° and virtual field of 55 kV/cm. The solid lines give the variation of phase with depth into the crystal for ten successive and equally spaced time samples. The dashed lines are the corresponding "effective phase shifts", where ϕ_{eff} is a measure of the displacement of a straight grating which would produce the same coupling, as determined by the program in Appendix E. This is the quantity which is measured by nulling the coupling using the PZT shifter and assuming no other variations in the shift take place.

8.2.2 Thermal Expansion

From the photocurrent measurements showing the pyroelectric current (Fig. 5.1) and the value of the pyroelectric constant (Appendix A) one can show that during these experiments the crystal heated up by several tenths of a degree centigrade. Heating the crystal by 0.5°C will expand it along the x-direction by about 1/20 of a grating wavelength. This expansion would take place mostly during the first minute of illumination, and therefore affect only the first reading (if any) in the present experiments. Thermal expansion and contraction may explain the lack of success met with initially in this work in attempts to study coupling at regular intervals during writing by decreasing the beam intensity before adjusting the PZT shifter so as not to write while shifting.

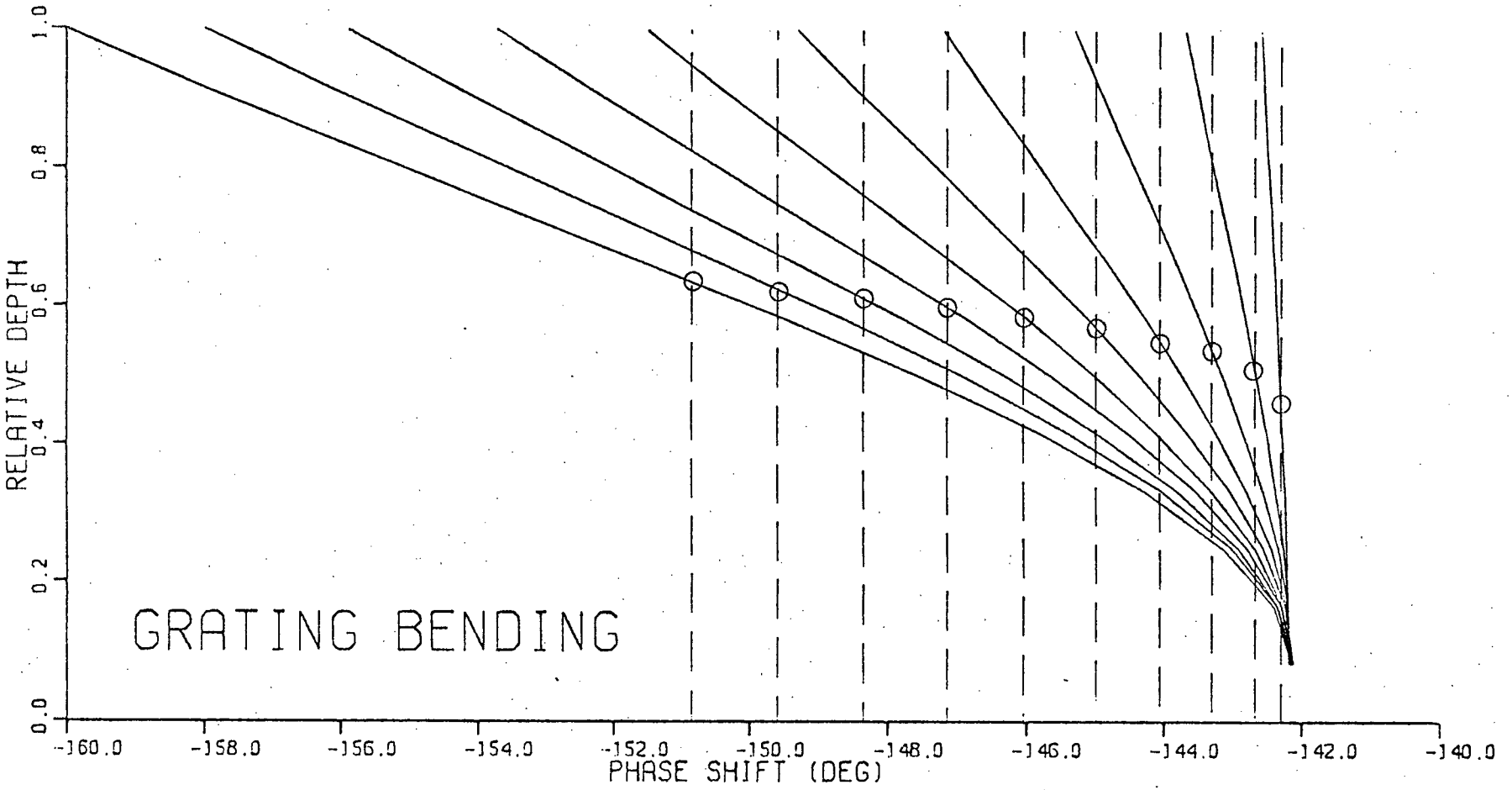

FIGURE 8.7

Time development of hologram curvature:

solid lines - curves generated by Moharam's model (see Appendix E)

dashed lines - effective displacement of equivalent simple grating

8.2.3 Bulk Motion of Crystal and Optical Components

As shown by the slopes in Fig. 8.4, the variation of phase with time can be caused by a sideways (x-axis) motion of the crystal of about 10nm/min. Motion of the mirror and lenses in the optical system may result in an equivalent effect by shifting the fringe pattern. Direct measurement of the motion of the fringe pattern from the Michelson Interferometer (Fig. 7.1) shows that such motion persists for days after the adjustment of the position of any component in the beam path due to the residual mechanical creep of the components.

The effect of the above problems is to give the $\phi(\varepsilon)$ lines in Fig. 8.4 a non-zero slope. Because this slope was the result of uncontrollable and quantitatively unpredictable processes, the coupling that follows from it is also unpredictable. This accounts for the wide variation in results in Fig. 8.5. However, as seen in Fig. 8.4, this is due to the phase shift undergoing a linear change with increasing time (or exposure) instead of remaining constant. Extrapolation back to t=0 gives a figure for the phase shift of the initially straight grating before the above mentioned processes have had a chance to cause a change in the relative positions of the grating and fringe pattern. A linear regression of the phase nulling voltage data (from which the lines in Fig. 8.4 were obtained) gives the value $\phi_o = 5.0° \pm 0.7°$.

Because it is a direct measurement of the phase shift, the line given by the PZT phase shifter is the more reliable of the two. The line obtained from equations 3.8 and 3.9 gets progressively less accurate as the grating departs from the "simple" grating geometry assumed in the derivation of the equations. In any case, the two methods agree at t=0 to within $\pm 1.4°$.

Fig. 8.8 is a graph of the coupling which would be expected for the case of $\phi(t=0) = 25°$ and $d\phi/dt = -10, -5, 0, 5$ and 10 degrees per unit time.

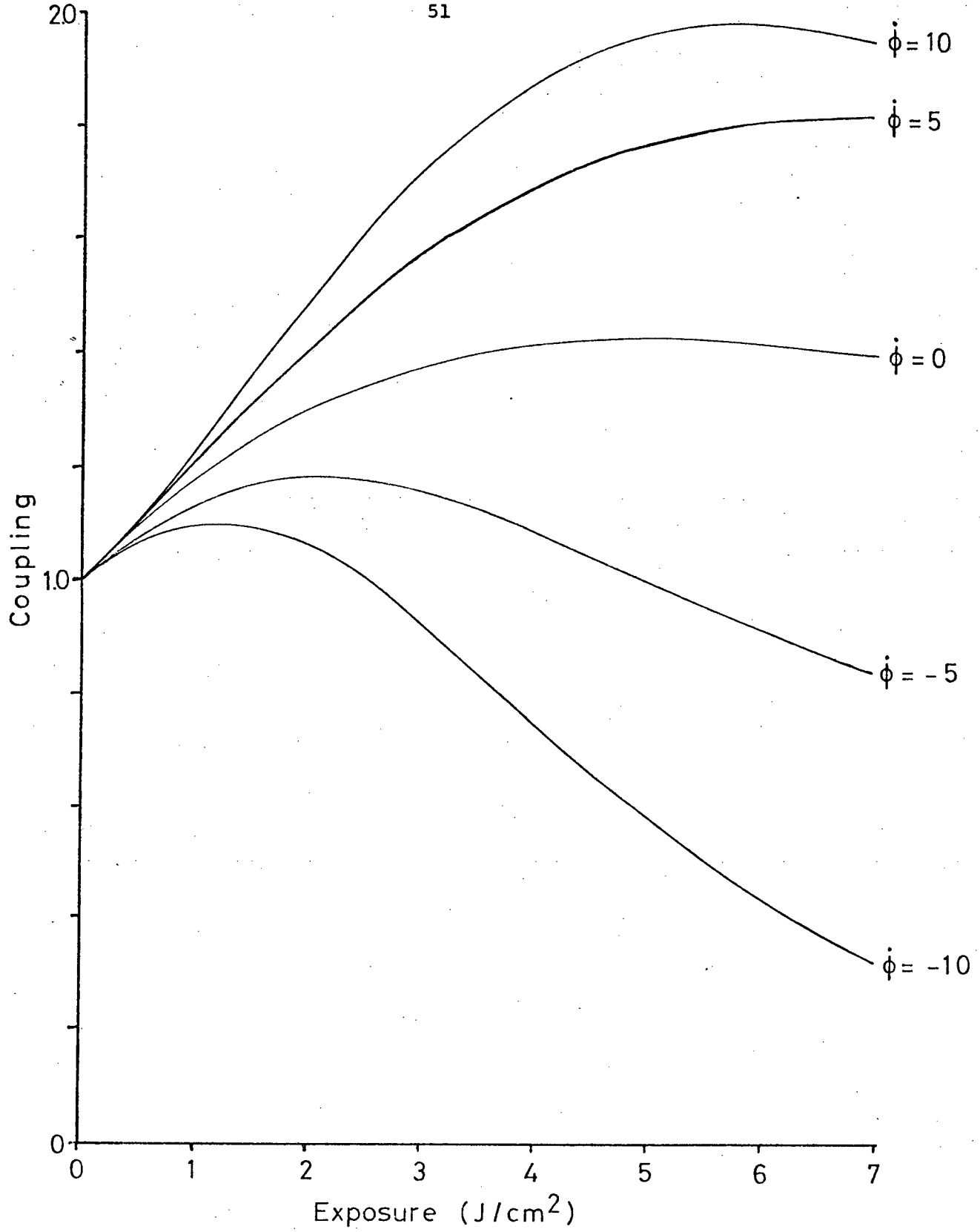

FIGURE 8.8

Simulated coupling for cases where $\phi_o = 25°$ and for various values of $\dot{\phi}$ $\left(\text{deg}/(\text{J/cm}^2)\right)$.

The crossover shown in the first two cases was occasionally observed during an experimental run, indicating that the creep was in the direction opposite to the phase shift due to the bulk photo-voltaic effect. This was sometimes strong enough to give the impression of reversed coupling.

8.3 Calculation of Photovoltaic Transport Length

Young et al. (1979) used the observed diffraction efficiency and the measured ratio of the exciting beam intensities at an exposure of 1.2 joules/cm^2 to calculate the phase shift using equations 3.8 and 3.9, and arrived at a figure of 10.4°. From this they obtained a value for the photo-voltaic transport length, L_p, of 24nm.

These calculations can now be repeated for the present set of data using $\phi_o = 5.0°$. The total phase shift is given by

$$\phi_o = \phi_p + \phi_D$$

$$= \tan^{-1}(\kappa L_p) + \tan^{-1}(E_D/E_v)$$

where

$E_D = \frac{k\kappa T'}{q}$ is the diffusion equivalent field,

$E_v = 45 \pm 5k$ V/cm^2 is the virtual field.

From this we can show that $L_p = 13\text{nm} \pm 3\text{nm}$. The difference between this value and that obtained by Young et al. (1979) can be explained by a possible drift in the phase shift during the time taken for the exposure to reach 1.2 joules/cm^2 in their experiment.

To restate the results of this chapter, the electron transport length due to the bulk photovoltaic effect, L_p, has been measured as 13nm. This manifests itself in the hologram as a displacement of the written grating along

the +c-axis with respect to the light fringe pattern, which in turn gives rise to beam coupling between the transmitted reference and subject beams.

9. SUMMARY

Studies of the hologram writing process in ferroelectric crystals and models to predict their evaluation in time and space centre around observations of the time development of the diffraction efficiency and beam coupling. Though considerable success has been achieved in predicting the former quantity in computer models, no such success has met attempts to match experiment with model predictions of the development of coupling. Consequently, some difficulty has been encountered in the calculation of such parameters as the photovoltaic transport length, as this requires an experimental determination of the phase shift which gives rise to the coupling.

The present work has been aimed at measuring the phase shift directly through the use of a PZT phase shifter and comparing this to calculations of the shift from the measured diffraction efficiency and beam coupling. It has been shown that the shift between the grating and fringe pattern does not remain a constant quantity during the writing process. This variation is due to processes which can be neither completely controlled nor quantitatively predicted. However, the variation (at least with the apparatus used in these experiments) is nearly linear, and it was found that both methods of measuring the phase shift yield the same result when the best-fit lines are extrapolated to t=0. This intercept gives the value of the phase shift before it has been affected by the several processes which later disguise the original value. For the $LiNbO_3$ crystal used, a phase shift due to the bulk photovoltaic effect of 2.9° was obtained, which corresponds to a transport length of about 13nm.

To establish the generality of this analysis it would be useful to make measurements on several crystals of different doping and under a variety of conditions. In any case, it is clear that without apparatus designed to

hold the optical components very still for periods of several minutes or hours it will not be possible to match up experimental results with computer model predictions of the coupling.

BIBLIOGRAPHY

Cathey, W. Thomas: Optical Information Processing and Holography. John Wiley and Sons (1974).

Caulfield, H.J. (editor): Handbook of Optical Holography (ch. 10). Academic Press (1979).

Chanussot, G: Ferroelectrics 8, p. 671 (1974).

Channussot, Fridkin, Godefroy and Jannot: App. Phys. Lett. 31, p. 3 (1977).

Chen, F.S.: J. App. Phys. 40, p. 3389 (1969).

Chen, LaMacchia, Fraser: App. Phys. Lett. 13, p. 223 (1968).

Clark, Disalvo, Glass, Peterson: J. Chem. Phys. 59, p. 6209 (1973).

Collier, Burckhardt and Lin: Optical Holography. Academic Press, Inc. (1971).

Cornish, William D.: The Photorefractive Effect in Lithium Niobate. Ph.D. thesis, Dept. of Elec. Eng., U.B.C. (1975).

Cornish, Moharam and Young: J. Appl. Phys. 47, p. 1479 (1976).

Dischler, Rauber: Solid State Comm. 17, p. 953 (1975).

el Guibaly, Fayez H.F.: The Photorefractive Effect in Lithium Niobate and its Applications. Ph.D. thesis, Dept. of Elec. Eng., U.B.C. (1979).

Fridkin, V.M.: Appl. Phys. 13, p. 357 (1977).

Glass, von der Linde, Negran: App. Phys. Lett. 25, p. 233 (1974).

Glass, von der Linde, Auston and Negran: J. Electr. Mat. 4, p. 915 (1975).

Jacobs, Sargent, Sculley: Adaptive Optics and Short Wavelength Sources (vol. 6 of "Physics of Quantum Electronics"). Addison-Wesley Publishing Co., Inc. (1978).

Johnston, W.D.: J. App. Phys. 41, p. 3279.

Koch, Munser, Ruppel, Wurfel: Ferroelectrics 13, p. 305 (1976).

Kogelnik, H.: Bell Tel. Tech. J. 48, 2909 (1969).

Kukhtarev, Markov, Odulov: Opt. Commun. 23, p. 338 (1977).

Marcatelli, E.A.J.: Appl. Opt. 19, p. 1468 (1980).

Marom, Friesem, Wiener-Avnear (editors): Applications of Holography and Optical Data Processing. Pergamon Press (1976).

Mikami, Ishida: Opt. Comm. 9, p. 354 (1973).

Moharam, M. Gamal: Hologram Storage by the Photorefractive Effect. Ph.D. thesis, Dept. of Elec. Eng., U.B.C. (1978).

Moharam, Gaylord, Magnusson, Young: J. Appl. Phys. 50, p. 5642 (1979).

Ninomiya, Y.: J. Opt. Soc. Am. 63, p. 1124 (1973).

Nye, J.F.: Physical Properties of Crystals (7th printing). Oxford University Press (1976).

Ohmori, Yamaguchi, Yoshino, Inuishi: Japan J. App. Phys. 16, p. 181 (1977).

Peterson, Glass, Negran: App. Phys. Lett. 19, p. 130 (1971).

Peterson, Glass, Carnevale, Bridenbaugh: J. Am. Ceram. Soc. 56, 278 (1973).

Phillips, Amodei, Staebler: RCA Rev. 33, p. 94 (1972).

Smith, H.M. (editor): Holographic Recording Materials (vol. 20 of "Topics in Applied Physics"). Springer-Verlag (1977).

Smith, Fraser, Denton, Rich: J. App. Phys. 39, p. 1600 (1968).

Staebler, Amodei: Ferroelectrics 3, 107 (1972a).

Staebler, Phillips: App. Opt. 13, p. 788 (1972a).

Staebler, Amodei: J. App. Phys. 43, 1042 (1972b).

Staebler, Phillips: App. Phys. Lett. 24, p. 268 (1974b).

Tamir, T. (editor): Integrated Optics (2nd ed.) (vol. 7 of "Topics in Applied Physics"). Springer-Verlag (1979).

Turner, E.H.: Appl. Phys. Lett. 8, p. 303 (1966).

von Baltz, R.: Phys. Stat. Sol. (b) 89, p. 419 (1978).

von der Linde, Glass and Rogers: Appl. Phys. Lett. 25, p. 155 (1974).

von der Linde, Glass and Rogers: Appl. Phys. Lett. 26, p. 22 (1975a).

von der Linde, Glass: Appl. Phys. 8, p. 85 (1975b).

von der Linde, Glass: Ferroelectrics 10, p. 5 (1976).

Young, Wong, Thewalt, Cornish: Appl. Phys. Lett. 24, 264 (1974).

Young, Moharam, El Guibaly, Lun: J. Appl. Phys. 50(6), 4201 (1979).

APPENDIX A

$LiNbO_3$ Crystal Data

A.1 Sources of Crystals

The crystals used in this work were commercially prepared by Crystal Technology Inc., Mountain View, California, and by Harshaw Chemical Co., Solon, Ohio. They were grown by the Czochralski technique, in which a poling electric field is applied and the boule is rotated as it is withdrawn from the melt. The composition of the melt is either stoichiometric or congruent, where the former contains more Li than the latter (49.0 mole% LiO_2 vs. 48.6 mole% LiO_2 respectively). Table A-1 lists the relevant data for each crystal used. It should be realized that over the past five years or so, these crystals have been subject to a number of processes, not always of a well recorded nature, and as a result can exhibit characteristics which may not be reproducible in another nominally identical crystal.

A.2 Miscellaneous Properties

Lithium niobate is a ferroelectric crystal with a distorted perovskite structure (ABO_3). As a stable ferroelectric at room temperature, it exhibits an electric dipole moment even in the absence of an electric field. If heated above its transition temperature, or Curie point (T_c = 1470° k for $LiNbO_3$) it loses its moment. Below T_c, the degree of polarization can be made to vary along a hysteresis loop as the externally applied field is varied (difficult at low temperature). The crystal has a rhombohedral structure (point group 3m with $a = .5499$, $\alpha = 55°52'$) (Nassau et al., 1966), and covalent bonds predominate. It can be thought of as being composed of sheets of oxygen in approximately hexagonal close packing with the resulting octahedral interstices being one-third occupied by Li, one-third by Nb, and the remaining one-third empty. There are

two separate values each for the Li-O and Nb-O distances. The present set of experiments was done with light of λ = 514.5nm, which falls within the region of relative transparency between 350nm and 5000nm. The indices of refraction at 500nm and 25°C are n_o = 2.34 and n_ε = 2.24. The dielectric constants are ε_r = 78 (perpendicular to c-axis) and e_r = 32 (parallel to c-axis). The pyroelectric coefficient is 10^{-2} $\mu C/(m^2 deg)$ at 100°C. It melts at 1260°C and has coefficients of expansion of 16.7 x 10^{-6}/deg C. along the a-axis and 2 x 10^{-6}/deg C. along the c-axis.

A.3 Electro-optic Behaviour

It is usually sufficient to consider the permittivity coefficients of a crystal to be constants, unaffected by the strength of an applied electric field. However, it is the case for some crystals (including $LiNbO_3$) that there is a small but detectable higher-order effect whereby readily attainable fields cause a change in the permittivity. At optical frequencies this is equivalent to a change in the index of refraction, and is the basis of the electro-optic effect.

The general tensor expression for the dielectric properties of an anisotropic crystal at optical frequencies is

$$D_i = \varepsilon_o \varepsilon_{ij} E_j$$

where ε_{ij} is the tensor relative permittivity relating the applied electric field E to the dielectric displacement D. Both the polarization and direction of propagation with respect to the crystal axes affect the propagation of an electromagnetic wave in a crystal, and in general two waves of different velocities may propagate for a given wave normal. Their refractive indices may be found by the ellipsoid, called the optical indicatrix, defined by the following equation:

$$\left(\frac{x_i}{n_i}\right)^2 = 1 \quad , \quad n_i = \sqrt{e_{ii}} \quad (e_{ii} \text{ of diagonalized matrix})$$

where we have used the Einstein summation convention that any index which occurs twice in the same term is to be summed. If the ellipsoid is cleaved through its centre perpendicular to the wave normal, the lengths of the axes of the resulting ellipse yield the directions of polarization of the two waves (see Figure A-2). The presence of an electric field results in deformation of the indicatrix, which is now defined by the equation (eq. A.1)

$$\left(n_{ij}^{-2} + z_{ijk}E_k + R_{ijk\ell}E_kE_\ell + \ldots\right) x_i x_j = 1 \qquad i,j,k,\ell = 1,2,3$$

where z_{ijk} and $R_{ijk\ell}$ are the linear and quadratic electro-optic coefficients. Because third and fourth rank tensors are inconvenient to write out, contractions to second rank form are performed according to the following conventions:

$$r_{mk} \longleftarrow z_{(ij)k}$$

$$R_{mn} \qquad R_{(ij)(k\ell)}$$

where m,n = 1,2,...,6 and m is related to ij and n to kℓ by the rules 1→11, 2→22, 3→33, 4→23, 5→13, 6→12. We are interested in the specific case of $LiNbO_3$, which is a uniaxial crystal exhibiting the electro-optic effect. Its high degree of symmetry results in most of the electro-optic coefficients r_{mk} being zero, and the rest being interdependant. The matrix form and numerical values of its elements are (Turner 1966)

Crystal Number(1)	Dimension (mm) a	b	c	Polished Faces	Iron Doping (mole %)	Composition of the Melt
1	15(2)	3	20	b	undoped	congruent
6	1(3)	10	10	a	0.1%	stoichiometric

(1) according to numbering of El Guibaly (1979).
(2) broken - half used was 7 × 3 × 20 mm.
(3) nominal - actual measurement is 0.69 mm.

FIGURE A-1: Table of Crystal Data

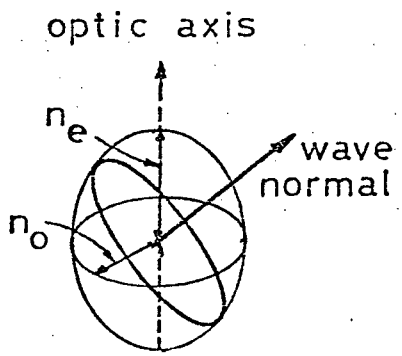

FIGURE A-2

The indicatrix for a positive uniaxial crystal.

FIGURE A-3

Application of an electric field E_3 to alter the indices of refraction seen by a wave propagating in the x_1 direction.

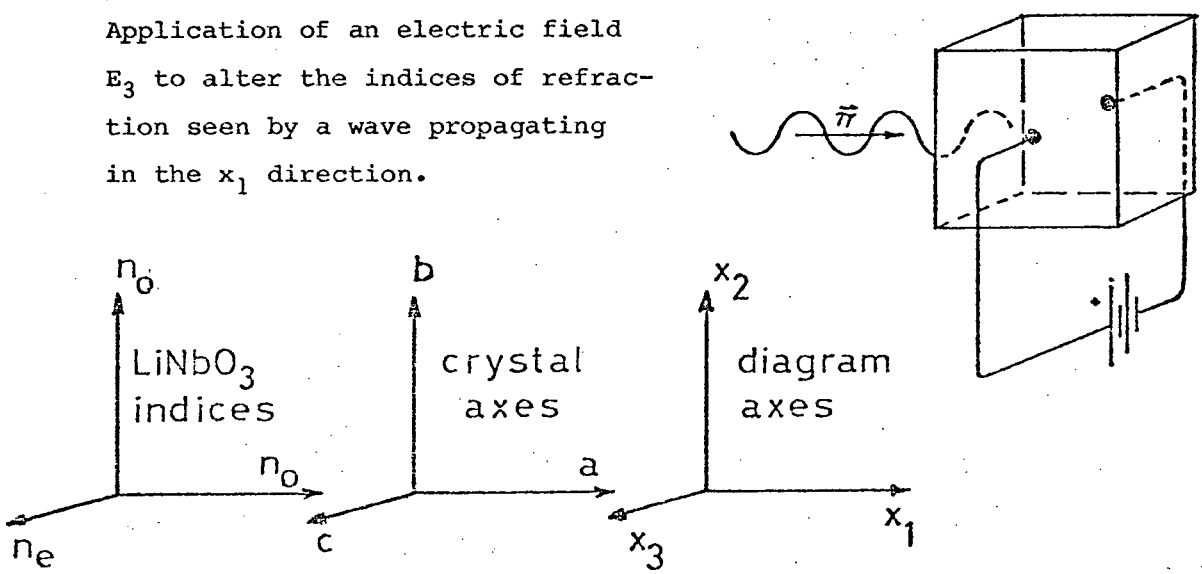

$$\begin{bmatrix} 0 & -r_{22} & r_{13} \\ 0 & r_{22} & r_{13} \\ 0 & 0 & r_{33} \\ 0 & r_{42} & 0 \\ r_{12} & 0 & 0 \\ -r_{22} & 0 & 0 \end{bmatrix}$$

$r_{13} = 8.6 \times 10^{-10}$ cm/Volt
$r_{22} = 3.4 \times$ "
$r_{42} = 28 \times$ "
$r_{33} = 30.8 \times$ "

The fact that $LiNbO_3$ is uniaxial can be used to obtain the index change to the applied field for the special case of a wave propagating in the x_2 direction through a crystal with the field applied in the x_3 direction (see Figure A-3). Because the indicatrix here is an ellipsoid of revolution, two of the principal axes are equal:

$$n_0 = n_1 = n_2$$

$$n_\varepsilon = n_3$$

The indicatrix (eq. 1) thus reduces to

$$(n_o^{-2} - r_{22}E_2 + r_{13}E_3)x_1^2 + (n_o^{-2} + r_{22}E_2 + r_{13}E_3)x_2^2$$
$$+ (n_e^{-2} + r_{33}E_{33})\, x_3^2 + 2(-r_{22}E_1)x_1x_2$$
$$+ 2(r_{42}E_2)x_2x_3 + 2(r_{42}E_1)x_3x_1 = 1 \qquad (A.2)$$

For our case, $E_1 = E_2 = 0$ and thus the above reduces to

$$(n_o^{-2} + r_{13}E_3)x_1^2 + (n_\varepsilon^{-2} + r_{33}E_3)x_3^2 = 1 \qquad (A.3)$$

If we consider field E_3 as effecting changes Δn_o and Δn_ε in the refractive indices, we could write

$$(n_o + \Delta n_o)^{-2}\, E_3\, x_1^2 + (n_\varepsilon + \Delta n_\varepsilon)^{-2}\, E_3\, x_3^2 = 1 \qquad (A.4)$$

Equating the coefficients of x_1^2 in (3) and (4) and solving for Δn_o, we get

$$\Delta n_o = -\frac{n_o^3 r_{13} E_3}{2}$$

and similarly for the x_3^2 coefficients we get

$$\Delta n_\varepsilon = -\frac{n_\varepsilon^2 r_{33} E_3}{2} \quad .$$

This simple formula for the index change also points out the linear relation between Δn and the applied field E for this special case.

APPENDIX B

Piezoelectric Phase Shifter

As shown in Figure 7.1, the phase relationship between the object and reference beams was altered by applying a voltage to the piezoelectric disc upon which the reference beam mirror was mounted. An explanation of the effect and details of the device follow.

i) Basic Piezoelectric Theory

Certain crystals develop an electric moment upon application of mechanical stress, with the moment being linearly proportional to the stress. This is called the "direct piezoelectric effect", and the complementary phenomenon, i.e. the application of an electric field to change the shape of the crystal, is referred to as the "converse piezoelectric effect". Mathematically, the piezoelectric effect can be represented by a third rank tensor d_{ijk} relating the stress and polarization. The state of stress, σ, of a crystal is completely specified by a second rank tensor of nine components, σ_{jk} $(j,k = 1,2,3)$, where a specific component σ_{jk} refers, for instance, to a force applied in the j direction across the faces perpendicular to the k direction, as in Figure B.1.

The polarization of a crystal is a vector quantity of three components, P_i. In the general case, each of these three components is a function of all nine stress components. For instance, in the 1 direction, the polarization is given by

$$P_1 = d_{1jk}\,\sigma_{jk} \qquad (j,k = 1,2,3) \tag{B.1}$$

and thus the general expression for all three directions of polarization is

$$P_i = d_{ijk}\,\sigma_{jk} \tag{B.2}$$

FIGURE B.1

The stress tensor element σ_{jk} refers to a force in the j direction across faces perpendicular to the k direction.

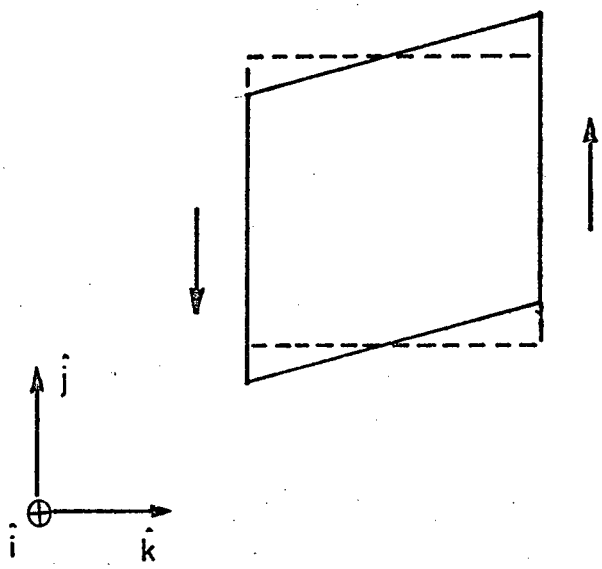

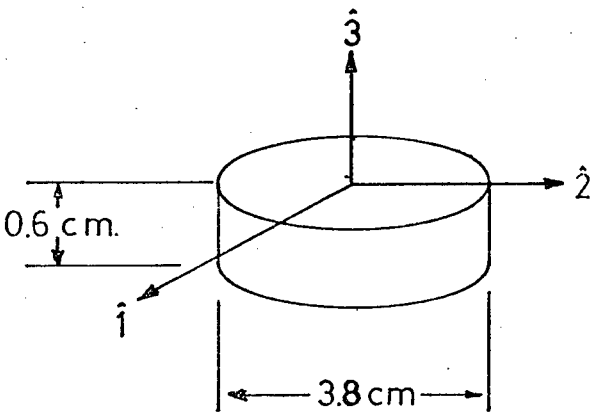

FIGURE B.2

Shape and dimensions of the Vernitron piezoelectric element.

where d_{ijk} represents the 27 piezoelectric moduli. In practice, crystal symmetry often renders many of the d_{ijk} interdependent, so that fewer than 27 numerical values need be considered. Equation B.2 implies that if a tensile stress, σ_{jk}, is changed to an equal and opposite stress, $-\sigma_{jk}$, the effect is to reverse the sign of polarization. Furthermore, unstated in eq. B.2 is the fact that, in the case of the crystal having a spontaneous polarization P_i^0 present in the absence of any stress, the P_i in eq. B.2 must be thought of as a change effected in the total polarization. If we ignore body torques, it is impossible to apply a stress σ_{ij} without also applying the opposite stress σ_{ji}, and so we can only physically measure their sum. It is conventional (and can be shown to be necessary) to set $d_{ijk} = d_{ikj}$ as a result of this, and thus the number of independent coefficients is reduced from 27 to 18. A further simplification of the mathematical representation is achieved by reducing the number of subscripts from 3 to 2 according to the following convention: the first subscript remains the same, but the second and third are replaced by a single digit according to the rule:

11 → 1	23 → 4
22 → 2	31, 13 → 5
33 → 3	21, 12 → 6

Factors of 1/2 are also introduced into the d_{ij} where j = 4,5,6. For consistency, we make equivalent changes to the stress tensor to get

$$\begin{matrix} \sigma_1 & \sigma_6 & \sigma_5 \\ \sigma_6 & \sigma_2 & \sigma_4 \\ \sigma_5 & \sigma_4 & \sigma_3 \end{matrix} \qquad \text{i.e. } \sigma_{j,k} \rightarrow \sigma_j \ , \ j = 1,\ldots,6$$

In this new 2-subscript notation, the piezoelectric moduli take the form of the matrix:

$$\begin{bmatrix} d_{11} & d_{12} & d_{13} & d_{14} & d_{16} \\ d_{21} & & & & d_{26} \\ d_{31} & & \text{etc.} & & d_{36} \end{bmatrix}$$

The relation B.2 is now written

$$P_i = d_{ij}\sigma_j \qquad i = 1,2,3 \qquad j = 1,2,\ldots,6$$

In the experiments dealt with here, the converse piezoelectric effect is used, and we note that it can be shown (Nye, p. 115) that the coefficients relating stress and polarization in the direct effect are the same as those relating field and strain in the converse effect. Thus the analogue of eq. B.2 is

$$\varepsilon_{jk} = d_{ijk} E_i \quad .$$

This too can be expressed in matrix notation by effecting the following substitution for the strain components:

$$\begin{bmatrix} \varepsilon_{11} & \varepsilon_{12} & \varepsilon_{13} \\ \varepsilon_{21} & \varepsilon_{22} & \varepsilon_{23} \\ \varepsilon_{31} & \varepsilon_{32} & \varepsilon_{33} \end{bmatrix} \longrightarrow \begin{bmatrix} \varepsilon_1 & {}^1/_2\varepsilon_6 & {}^1/_2\varepsilon_5 \\ {}^1/_2\varepsilon_6 & \varepsilon_2 & {}^1/_2\varepsilon_4 \\ {}^1/_2\varepsilon_5 & {}^1/_2\varepsilon_4 & \varepsilon_3 \end{bmatrix}$$

and then writing

$$\varepsilon_j = d_{ij} E_i \qquad i = 1,2,3 \qquad j = 1,2,\ldots,6$$

ii) The "Vernitron" Lead Zirconium Titanate Piezoelectric Element

The piezoelectric phase shifting element used in these experiments was a poled, thickness-expanding sintered ceramic disc of lead zirconium titanate (PZT) with dimensions and conventional axes as shown in Fig. B.2. The piezoelectric coefficient given in the Vernitron spec sheet is $d_{33} = 285$ pm/V ± 20%, which relates the strain in the 3 direction to the applied voltage in the

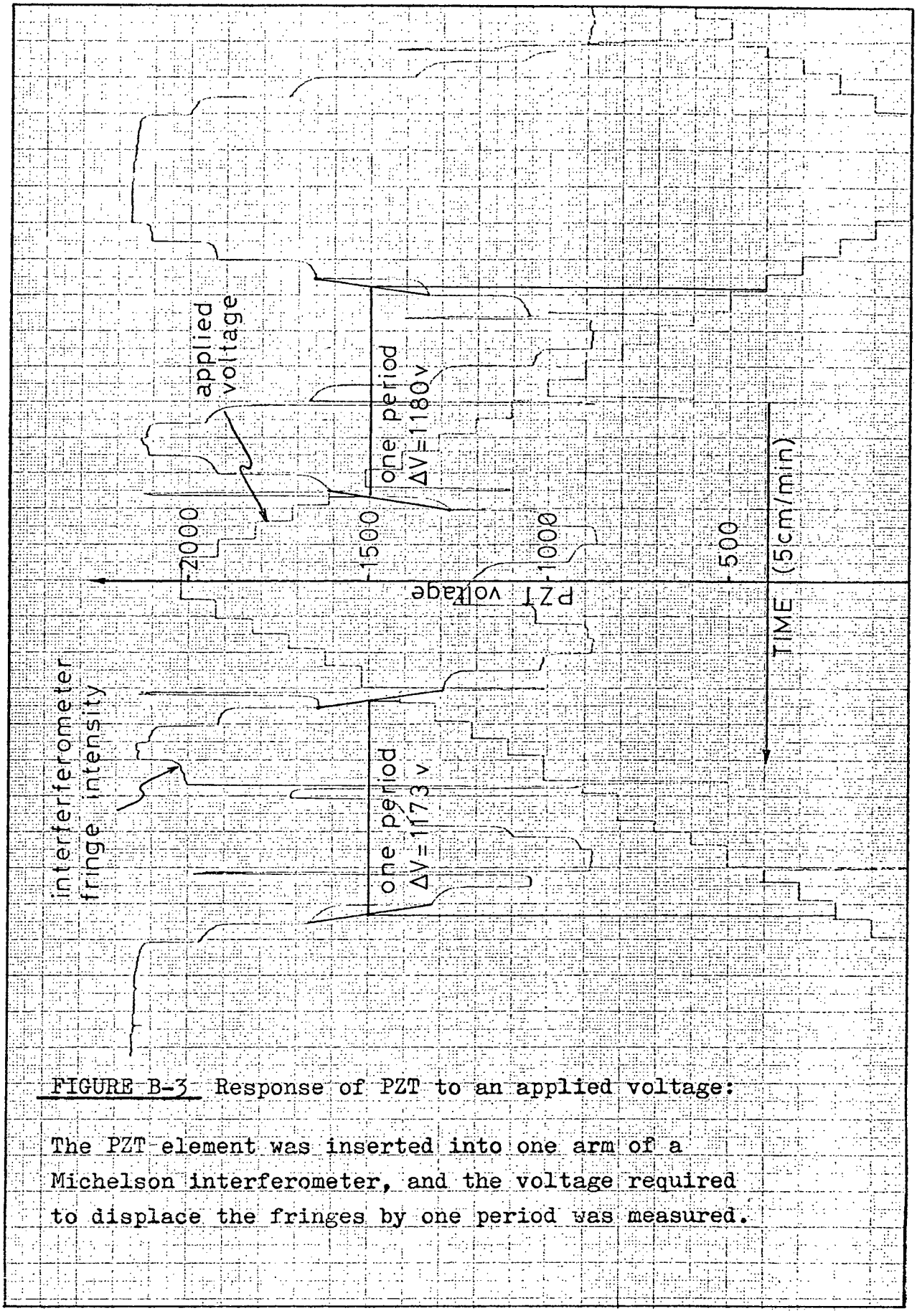

FIGURE B-3 Response of PZT to an applied voltage:

The PZT element was inserted into one arm of a Michelson interferometer, and the voltage required to displace the fringes by one period was measured.

3 direction. The value obtained in this lab using a Michelson Interferometer is d_{33} = 219 pm/V ± 2% (Fig. B.2).

A lower limit on the time required to step the voltage on the PZT and thereby study the coupling of the writing beams is set by the relaxation time of the PZT ceramic (Fig. B.3). That is, a change in voltage across the ceramic does not result in the ceramic immediately assuming its new dimensions, but rather initiates an approximately exponential approach to the new dimension. This is somewhat inconvenient as, during the relatively long time required to step the voltage through the required voltage range, the hologram being studied changes due to the continued writing of the gradually shifting fringe pattern. The obvious solution of reducing the beam intensity to inhibit writing during measuring ran into problems with thermoelectric effects, as mentioned elsewhere.

APPENDIX C

Michelson Interferometer
(PZT calibration, bench vibration)

In this work a Michelson Interferometer was used both to calibrate the PZT phase shifter and to check on the mechanical stability of the optical bench. Figure C.1 is a schematic diagram of the device geometry. If $|D_1-D_2|$ is less than the temporal coherence length of the laser, the two beams formed by the beam splitter (BS) and brought back together by the mirrors (M_1, M_2) will form a diffraction pattern. Variation in the distance $|D_1-D_2|$ will cause the pattern fringes to move as the interference becomes alternately constructive and destructive at any fixed point on the screen. If one of the mirrors is mounted on a PZT shifter, then varying the voltage on the shifter and counting the passage of fringes on the screen will provide a means of calibrating the piezoelectric constant of the shifter (see Appendix B).

Setting the interferometer up on the optical bench and observing the variation of fringe position provides a means to measure the degree of mechanical isolation offered by the bench. Three types of variation were noticed. The first was clearly due to building vibration (occupants, machinery) being transmitted to the optical componts by the bench, and was often accompanied by slamming doors, etc. This was minimized by conducting experiments at night. The second source of noise was random variations in the differential path length caused by air currents moving in the split beam paths and causing variations in the phase path lengths. This was minimized by covering the bench with a plexiglass greenhouse and further isolating the beams in cardboard tubing. The third type of variation in path length consisted of a slow monotonic increase or decrease in the differential path length with a speed of about one fringe per minute or so and gradually decaying over a period of days to a fringe per few

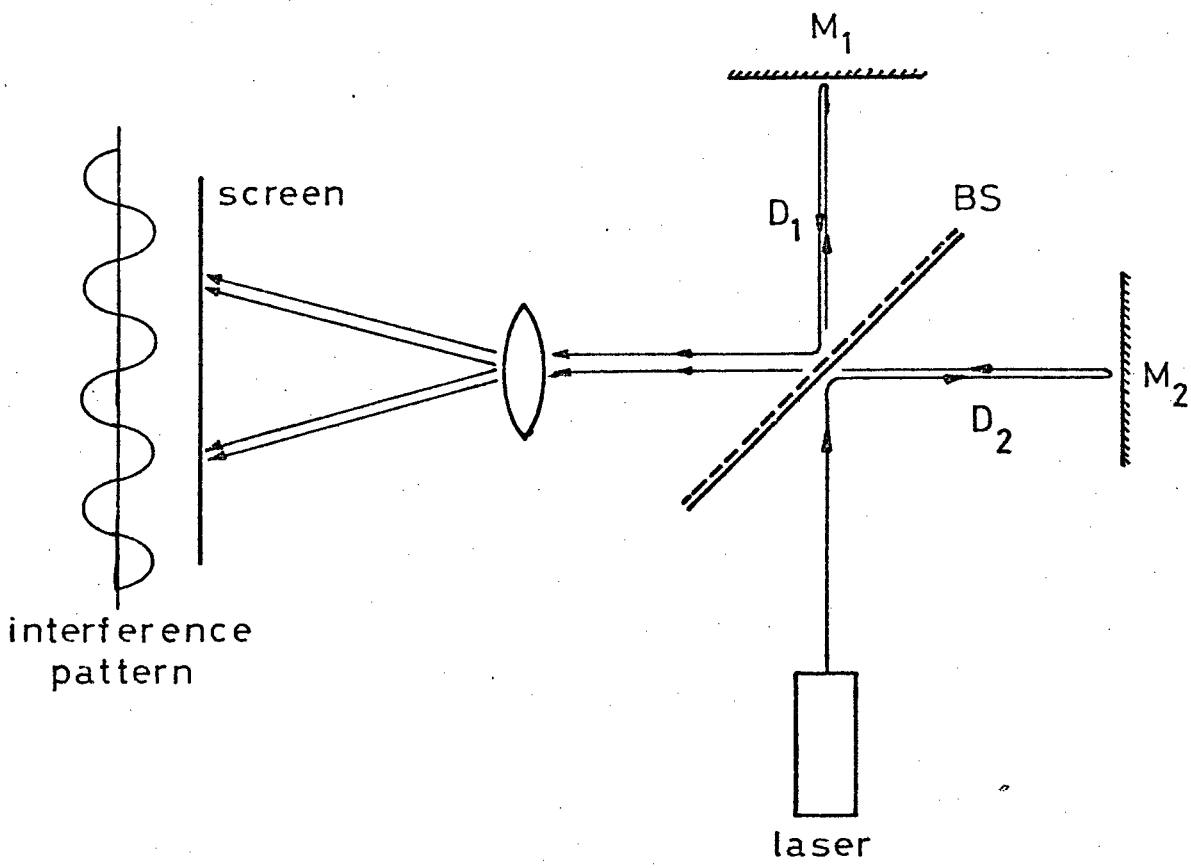

FIGURE C.1

Schematic of Michelson interferometer as used to detect bench vibration and to calibrate piezoelectric element.

hours. This was immediately evident every time the equipment was set up, and was attributed to a gradual relaxation of the mirror holders after the optics were properly aligned. This was treated by redesigning the PZT holder and also simply by waiting a few days after alignment before taking any serious measurements.

APPENDIX D

Applications of Holography

The storage of holograms in ferroelectric crystals is part of the larger field of modern optical technology currently undergoing rapid development in applications connected to general information handling. One example of the interfacing of holography to other new devices involves the real-time reconstruction of three-dimensional images using holographic techniques to mix wave components that have passed through long fibres (Tamir, p. 309). This would make use of both the high data rate attainable at optical frequencies and the relative immunity of optical signals to electromagnetic interference. Further applications of holographic techniques will be discussed and an example of a holographic computer memory given.

Desirable qualities in two-dimensional displays (e.g. 35mm slides) are high resolution, high image brightness, stored image durability, simplified processing and reduced cost of copies. It has been shown (Clay; in Caulfield) that 35mm slides can be considerably improved upon using focussed-image holograms, where an image of the object is formed by a lens on a recording medium and mixed with a reference beam.

Though the imagination can come up with many possible uses for three-dimensional displays, many of them appear not to be practical when carefully studied. It seems that the major potential use lies in the field of artistic endeavour, but artists have been slow to adopt this new technique, presumably because of its technical nature.

All of the classical interferometry setups have their analogs in holographic interferometry, with the latter allowing greatly expanded capabilities (Brandt; in Caulfield). These include the use of much larger aperture,

application to studies involving random or diffuse wavefronts, and potential for multiple exposure techniques (in vibration studies, for instance).

Pattern and character recognition are currently main areas of applied optical data processing. The aim here is to determine the presence and/or location of a reference pattern in an input image by examining the degree of correlation between an input and a reference function. The most common system performs the correlation by multiplying the Fourier transforms of the input and reference functions, where the latter is stored as the conjugate Fourier transform of the complex reference function (which is, in effect, a hologram).

Image processing (generally, the manipulation of multidimensional signals) involves image enhancement, information extraction, efficient coding, pattern recognition and computer graphics as they relate to interpreting aerial photographs and maps, medical, x-rays, television images, etc. Optical techniques alter higher information content handling ability, and may include the use of computer generated holograms, a study in itself (Catheg; Ch. 9).

Holography was originally invented to enhance electron microscope images. Although the bulk of holographic research has moved to other areas, limited success has been achieved with holographic microscopy (Cox; in Caulfield). Because a conventional microscope is designed to have a high transverse magnification at the expense of the depth of field, it is often difficult to see fine detail throughout a large volume. This can be overcome to some extent by making a hologram of an image at low magnification (and good depth of field) and later viewing it at high magnification with a conventional microscope. Time varying processes (e.g. crystal growth) can be detailed by taking two successive holograms and superposing them during construction.

A holographic optical element (HOE) can be designed to transform any single, entering wavefront into any other single, exiting wavefront. They offer the ability to provide unusual geometrical configurations or special

spectral characteristics, but this is usually accompanied by the addition of a large amount of aberration to the system (e.g. astigmatism and coma) to such an extent that "one should resort to the use of a HOE only when it is impossible to use conventional lenses and mirrors" (Close; in Caulfield). Examples are elements which must conform to an unusual shape such as a helmet visor, design of very large elements (in the spirit of a Fresnel lens), and where large surfaces of narrow spectral reflectivity must be used (as in aircraft "heads up" displays).

The considerable number of other applications of holographic techniques include: spectroscopy, especially at high speeds; contouring methods (2-D maps of 3-D objects); multiple image generation (e.g. for image recording or parallel optical processing) and particle size measurements.

Finally, we deal with the application which has received most attention in applied research; digital data storage. The need for larger, faster, and less expensive memories for data storage has led to the development of holographic memories in an attempt to capitalize on the potential of optical devices. We note in this regard the recent description of an optical subpicosecond gate (Marcatelli, 1980). Figures D1 and D2 give performance data on various devices in use as compared to holographic devices. It is seen that the trade-off between access time and storage capacity, and between access time and memory cost is less severe for holographic devices than the others listed. One can list four broad categories of memory; archival storage (large amounts of data occasionally accessed), read-mostly storage (similar to archival but capable of being occasionally altered), fast recording storage (for rapid storage of rapidly accumulated data to be read later), and fast read-write-erase memory (as in most computer memories).

A potentially high capcity, fast random access holographic memory of the type to be described may represent a solution to these varied needs, or

occupy a unique position in a hierarchical set of solutions. Initial design considerations (Hill, 1976) indicated that holographic memories would have these five basic features:

i) they would be Fourier transform holograms (as opposed to direct images) in order to protect against localized loss of data due to medium imperfections or surface dust;

ii) they would be in a 2-D page format, as the 3-D imaging capability of holograms offers no advantages;

iii) the information would be in binary code form as opposed to pictorial to allow for speed and ease of page composition and bit detection;

iv) analysis shows that thick phase holograms would be much more efficient than absorption or thin holograms;

v) moving mechanical parts would be eliminated to improve reliability.

A schematic of a 3-D storage system using a ferroelectric crystal is presented in Fig. D.3. The Bragg angle selectivity of such a medium is used to enable the superposition of multiple holograms (up to 500), so the address of a bit is XYΦ. The main optical components are the light source, beam deflectors, page composer, recording medium, and detector array.

The light source should provide intense (~1 Watt), collimated, coherent light pulsed or gated at about 1 MHz and in the blue or green part of the spectrum to take advantage of the λ^{-3} relationship between storage density and wavelength. The argon-ion gas laser meets these requirements, although it displays a low conversion efficiency of electrical power to optical power.

Fast and accurate beam deflectors are needed to position the laser beam for reading, writing and erasing operations. Acousto-optic and electro-optic deflectors are the main candidates, with the latter being faster but suffering light loss through surfaces and having a high cost. Because

electro-optic coefficients are too small to produce large deviations they are often cascaded to increase the effect. A digital electro-optic deflector may be constructed by cascading m deflectors to give 2^m deflection angles, and random access times of 0.8 μs. have been achieved.

The data input device is located in the object beam path and consists of an array of "open or shut" binary apertures which interfere with the reference beam to form a data matrix at the detector array. The requirements of this page composer are that it exhibit a high frame speed, high resolution, a high contrast ratio, stability, uniformity, and have full page addressing and a sufficiently large aperture to accomodate a large number of bits per page. A useful but slow liquid crystal page composer has been constructed by RCA (Labrunie et al., 1974). Among a number of alternate possibilities is the lead lanthanum zirconate titanate (PLZT) block data composer, which is faster than the liquid crystal version.

The recording material is a central component and determines to a large extent how flexible and efficient the entire system will be. The characteristics of the ideal medium are a high sensitivity and large diffraction efficiency to make maximum use of available light, long lifetime and nonvolatile storage, high resolution to provide high density storage, nondestructive readout, and an erase-rewrite capability. To date no material fulfills all of these requirements.

The array of photodetectors used to convert the holographically reconstructed data pattern into an electrical signal would consist of one sensing photodiode or phototransistor and one or two addressing switches for each bit. These photodiodes must exhibit high detectivity and be able to store incident optical energy for brief periods to allow readout by words. The array must allow complete random access to all words. The technology to construct large defect-

free arrays of this type already exists in the form of silicon-diode-array camera tubes.

Although the theoretical storage density for 2-D systems is of the order of λ^{-2}, and for 3-D of the order $(n/\lambda)^3$, practical limitations imposed upon the system by other factors decrease this limit. For instance, optical aperture effects put a lower limit on spot size, detector noise limits the number of bits per page, beam deflector resolution limits the number of XY addresses per page, and the medium recording range, image crosstalk and granularity all limit the number of holograms that can be superposed.

Several optical memories are commerically available. The first commerical nonmechanical optical memory was the Megafetch data processor introduced by 3M in 1974. It is a 50 Mbit read-only system capable of 15 Mbaud data rates, and uses a set of separate 2-D holographic data plates.

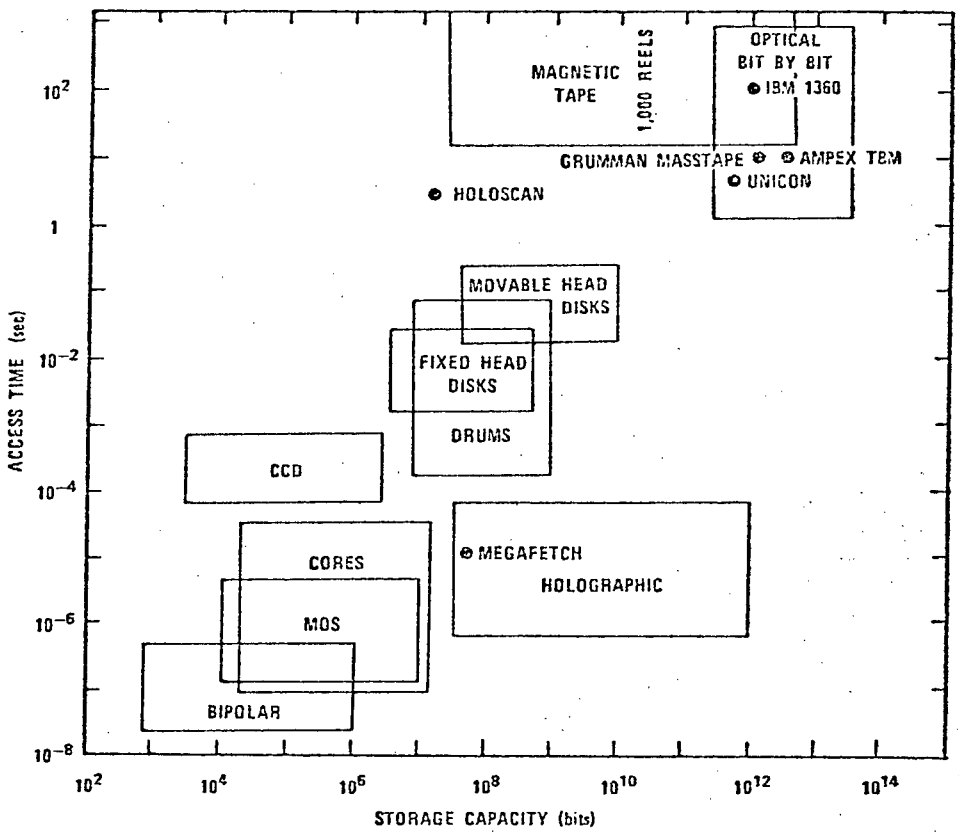

FIGURE D-1(a)

A comparison of various memory types in terms of access time and cost per bit of stored data. (from Caulfield)

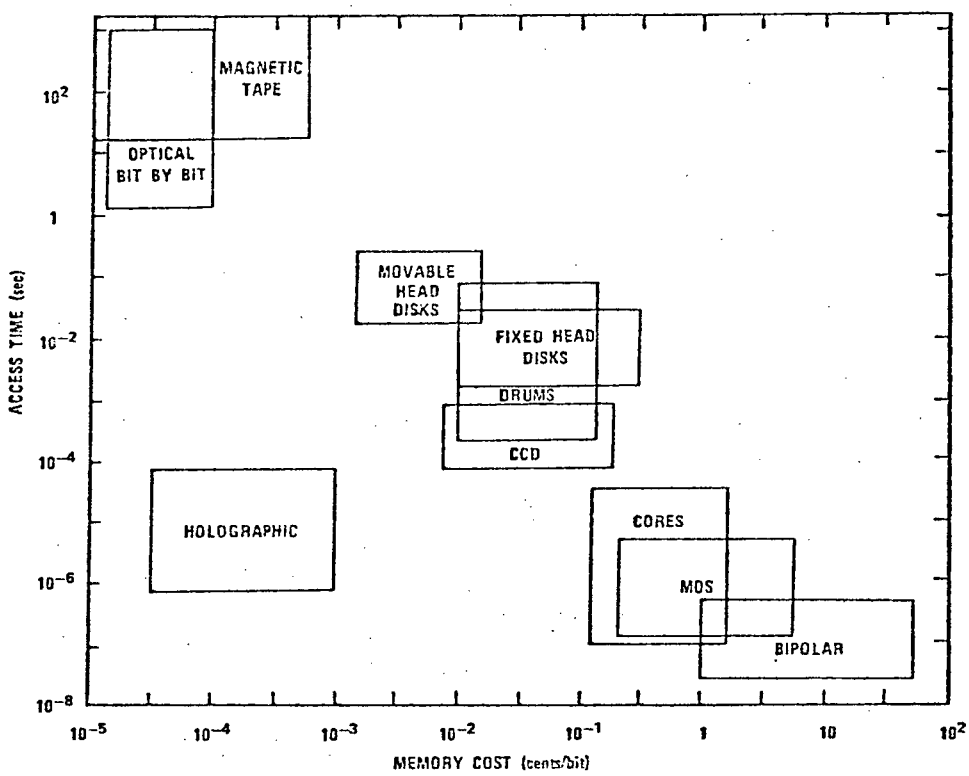

FIGURE D-1(b)

A comparison of various memory types in terms of access time and storage capacity. (from Caulfield)

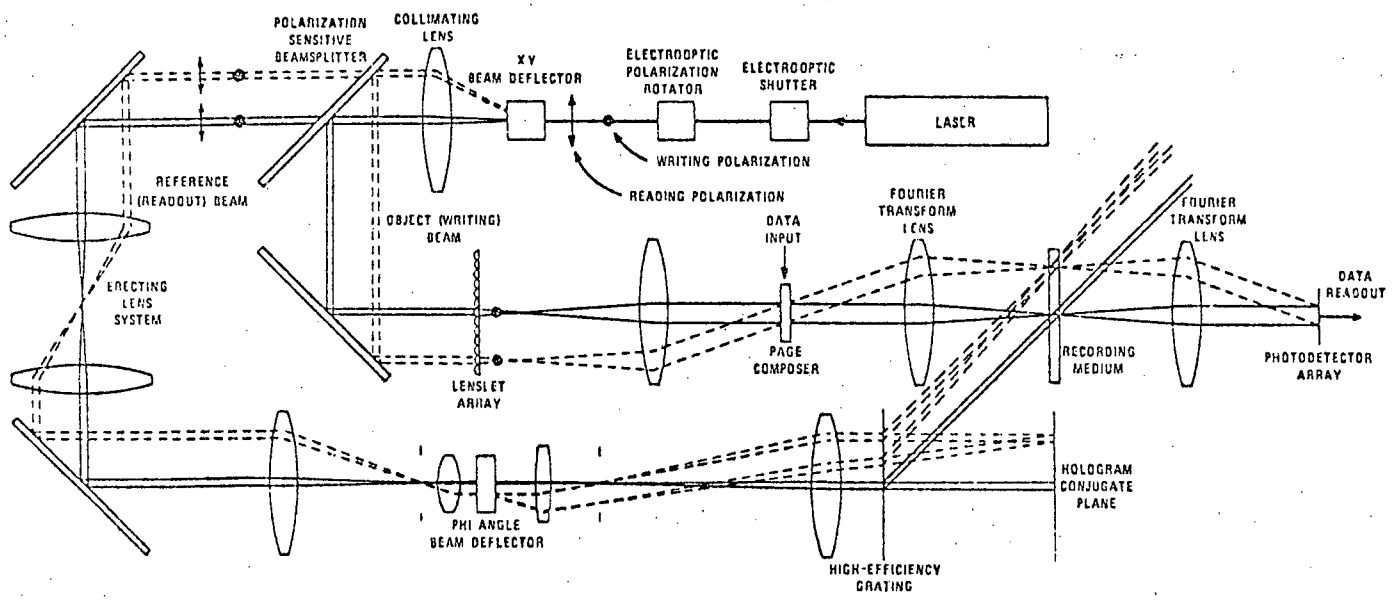

FIGURE D-2

A holographic optical memory system using three-dimensional (volume) storage. (from Caulfield)

APPENDIX E

A number of data reduction and simulation programs were used in this work. Among these was the hologram writing and read/erase program written by Moharam and modified by el Guibaly for the case of a non-zero but constant phase shift. This was slightly altered and used in this work to obtain the data for Figure 8.7 (solid lines), showing the time development of the grating curvature.

Two of the remaining programs are given here:

(1) "ZERO" is used to obtain the dashed lines in Figure 8.7, which shows the displacement of the straight line grating that would produce the same coupling as the corresponding curved grating.

(2) "EXPCUP" is used to generate the curves of Figure 8.8, which shows the sort of coupling curves which would arise for the case of a non-zero initial phase ϕ followed by a time variation in the phase ($d\phi/dt$ dds$\neq$0). ("SIMDAT" is a file holding the coupling and diffraction data measured from the experimental run shown in Figure 8.2.)

```
C
C-----------------------------------------------------
C                FILE: "ZERO"
C-----------------------------------------------------
C
C  'ZERO' INPUTS SELECTED DATA FROM 'HOLO3' (10 TIME
C  SAMPLES, 12 Z-SEGMENTS) DESCRIBING THE PHASE (PHIHG)
C  AND AMPLITUDE (AMP) OF THE BENT HOLOGRAM GRATING,
C  AND MOVES THE GRATING OVER TO A POSITION STRADDLING
C  THE FRINGE PATTERN SO THAT THE COUPLING IS NULLED
C  (I.E., THE EXITING R AND S BEAMS ARE SET EQUAL.)
C  AMPCON IS A CONSTANT CONVERTING THE FIELD AMPLITUDE
C  OUTPUT FROM 'HOLO3' TO INDEX VARIATION AMPLITUDE
C  FOR USE IN THE SUBROUTINE 'THRU'.
C  'DO 10' >> TIME STEPS

      REAL TIME(10), AMP(12,10), PHIHG(12,10), AMPV(12), PHIHGV(12)
      AMPCON=5.2E-6
      CALL MODEL(AMPCON,TIME,PHIHG,AMP)
         WRITE(5,1)
1        FORMAT(' TIME ',' EFFECTIVE SHIFT')
      DO 10 I=1,10
         DO 20 J=1,12
            AMPV(J)=AMP(J,I)
            PHIHGV(J)=PHIHG(J,I)
20          CONTINUE
         CALL EQUAL(PHIHGV,AMPV,PHIEQ)
         PHIEQD=PHIEQ*45./ATAN(1.0)
         WRITE(5,2) TIME(I),PHIEQD
2        FORMAT(' ',F4.2,F12.2)
10       CONTINUE
      STOP
      END


C*************************************************
      SUBROUTINE MODEL(AMPCON,TIME,PHIHG,AMP)

C  MODEL READS THE STORED OUTPUT FROM HOLO3 IN TWO 12X11
C  MATRICES (AP,F) WHICH GIVE INTERNAL FIELD AMPLITUDE
C  AND PHASE SHIFT, AND MULTIPLIES THEM BY CONSTANTS
C  "CONV" TO CONVERT THE PHASE TO RADIANS AND "AMPCON"
C  TO CONVERT THE FIELD AMPLITUDE TO AN INDEX AMPLITUDE.
C  "AMPCON" MUST BE GIVEN IN THE CALL STATEMENT.

      REAL TIME(10),PHIHG(12,10),AMP(12,10)
      DO 10 I=1,10
        READ(5,51) TIME(I),(PHIHG(J,I),J=1,12)
 51     FORMAT(F7.3,12(F8.3))
 10     CONTINUE
      DO 20 I=1,10
        READ(5,51) TIME(I),(AMP(J,I),J=1,12)
 20     CONTINUE
      CONV=ATAN(1.)/45.
      DO 30 I=1,10
        DO 40 J=1,12
          AMP(J,I)=AMP(J,I)*AMPCON
          PHIHG(J,I)=PHIHG(J,I)*CONV
 40       CONTINUE
```

```
 30      CONTINUE
       RETURN
       END


C*******************************************
       SUBROUTINE EQUAL(PHIHG,AMP,PHIEQ)

C  EQUAL DOES A SEARCH FOR THE PHASE ANGLE "PHIEQ" WHICH
C  WOULD RESULT IN NO COUPLING IF THE HOLOGRAM GRATING
C  WAS A SIMPLE LINEAR ONE.  I.E., IT IS THE "EFFECTIVE"
C  PHASE SHIFT OF THE GRATING MEASURED EXPERIMENTALLY
C  WHEN THE PZT VOLTAGE IS ADJUSTED FOR ZERO COUPLING.
C  "DO 10" >>SEARCH STEPS;    'DO 20" >> SHIFTS GRATING BY PHIEQ

       REAL PHIHG(12),AMP(12),PHIHGT(12)
       PHIGAP=(PHIHG(12)-PHIHG(1))/2.
       PHIEQ=PHIHG(1)+PHIGAP
       DO 10 I=1,13
         DO 20 J=1,12
           PHIHGT(J)=PHIHG(J)-PHIEQ
 20        CONTINUE
         CALL THRU(PHIHGT,AMP,RINT,SINT)
         PHIGAP=PHIGAP/2.
         IF(RINT.LT.1.0) PHIEQ=PHIEQ-PHIGAP
         IF(RINT.GT.1.0) PHIEQ=PHIEQ+PHIGAP
         IF(ABS(RINT-1.0).LE.0.0001) GO TO 11
 10      CONTINUE
 11    RETURN
       END


C*********************************************
       SUBROUTINE THRU(PHIHG,AMP,RINT,SINT)

C  "THRU" SENDS TWO BEAMS OF EQUAL AND UNIT STRENGTH AT +/- 19
C  DEGREES TO THE NORMAL THRU THE 12 LAYERS AND GIVES THEIR
C  INTENSITIES AT THE OUTPUT SIDE (RINT,SINT).  THE WAVELENGTH
C  IS 515.5 NM AND LAYER THICKNESS IS DZ. (SEE MOHARAM P74 FOR MATH)


       REAL AMP(12),PHIHG(12)
       COMPLEX R,S,RSTORE,CZT,SZT
       WL=514.5E-7
       DZ=.068/12.
       PI=4.*ATAN(1.0)
       THETA=19.*PI/180.

       R=CMPLX(1.,0.)
       S=CMPLX(1.,0.)
       DO 10 I=1,12
         RSTORE=R
         C=PI*AMP(I)/WL/COS(THETA)
         CZT=COS(C*DZ)
         SZT=SIN(C*DZ)
         R=R*CZT-(0.,1.)*S*SZT*
     &     CMPLX(COS(PHIHG(I)),-SIN(PHIHG(I)))
         S=S*CZT-(0.,1.)*RSTORE*SZT*
     &     CMPLX(COS(PHIHG(I)),SIN(PHIHG(I)))
 10      CONTINUE
```

```
      RINT=REAL(R*CONJG(R))
      SINT=REAL(S*CONJG(S))
      RETURN
      END

End of File

C*********************************************************
C FILE:"EXPCUP"  >> TO REDUCE 'SIMDAT' PARAMETERS.
C*********************************************************

      REAL RCUP(8),SCUP(8),RDIF(8),SDIF(8)
      CALL INPUT(RCUP,SCUP,RDIF,SDIF)
      CALL ANDAT(SDIF,RCUP)
      CALL SIMDAT(SDIF)
      STOP
      END

C-------------------------------------------------------
      SUBROUTINE INPUT(RCUP,SCUP,RDIF,SDIF)

C  INPUT READS DATA FROM FILE 'SIMDAT', NORMALIZES THE
C  FIGURES, AND PUTS THEM INTO THE PROPER VECTORS.

      REAL RCUP(8),SCUP(8),RDIF(8),SDIF(8)
      READ(5,51) (RCUP(I),I=1,8),(SCUP(I),I=1,8),
     1           (RDIF(I),I=1,8),(SDIF(I),I=1,8)
51    FORMAT (8F5.1)
      DO 10 I=1,8
         RCUP(I)=RCUP(I)*2./(RCUP(I)+SCUP(I))
         SDIF(I)=SDIF(I)/(SDIF(I)+RDIF(I))
10       CONTINUE
      WRITE(6,1) (SDIF(I),I=1,8),(RCUP(I),I=1,8)
1     FORMAT(' ','SDIF= ',8F7.3,/,' RCUP= ',8F7.3)
      RETURN
      END


C-------------------------------------------------------
      SUBROUTINE ANDAT(SDIF,RCUP)

C  "ANDAT" CALCULATES THE PHASE SHIFT FROM THE NORMALIZED
C  COUPLING AND DIFFRACTION EFFICIENCY FOR EACH DATA POINT.

      REAL SDIF(8),RCUP(8),PHI(8)
      DO 10 I=2,8
         PHI(I)=45./ATAN(1.0)*ARSIN((RCUP(I)-1.)/SIN(2.*ARSIN(SQRT(SDIF(I)))))
10       CONTINUE
      WRITE(6,1) (PHI(I),I=2,8)
1     FORMAT (' ',/,'PHI= ****.** ',8F7.2)
      RETURN
      END


C-------------------------------------------------------
      SUBROUTINE SIMDAT(SDIF)

C  "SIMDAT" STARTS WITH THE OBSERVED VALUES FOR THE
C  DIFFRACTION EFFICIENCY AND CALCULATES THE COUPLING
C  FOR VARIOUS VALUES OF PHI(T=0) AND D/DT (PHI)
```